A Computational Method for Full-Field Mechanics Imaging via the Self-Sensing Inverse Problem Enhanced with Sensor Data Fusion

Andrew L. Nguyen[a], Tyler N. Tallman[a]

[a]*School of Aeronautics and Astronautics, Purdue University, 701 W. Stadium Avenue, West Lafayette, 47907, IN, USA*

Abstract

Achieving material state awareness (MSA) of a mechanical system, structure, or component empowers engineers to be able to perform accurate failure prognosis and estimate remaining operational lifetime. Piezoresistive materials exhibit a change in electrical conductivity (or resistivity) when subjected to mechanical strain and therefore have the potential to enable functional, self-sensing structures that can provide real-time insight into their mechanical state. While piezoresistive materials have been demonstrated to be able to detect and localize damage by imaging conductivity changes, conductivity changes alone do not directly translate to stresses, strains, or displacements, values that are more meaningful for stress and failure analyses. To this end, the self-sensing inverse problem (SSIP) is a method which reconstructs the strain state that gives rise to an observed conductivity distribution. The SSIP has to date been computationally and experimentally demonstrated to reconstruct the deformed displacement field of simple geometries under load with reasonable accuracy, but mathematical limitations can make obtaining an accurate reconstruction difficult. In this work, we seek to improve the ability of the SSIP to obtain accurate displacement field reconstructions on more complex geometries by incorporating sensor data fusion (SDF) techniques. We herein develop a computational inverse problem for two SDF methods, one fusing electrical resistivity with displacement data and another fusing resistivity with strain data, and demonstrate these methods computationally on shapes representing aircraft components. These results show that incorporating data from relatively few displacement sensors allows the SSIP to reconstruct the displacement field with high accuracy. The results also demonstrate that incorporating strain sensor data improves the accuracy of the displacement reconstruction, though to a lesser degree than displacement data.

Keywords: self-sensing materials, computational inverse problems, finite element methods, sensor data fusion

1. Introduction

During operational use, the components, structures, and mechanisms of an engineering system will experience material degradation and damage. To ensure the continued safety and effective performance of the system, inspections and maintenance must be performed. For example, all commercial aircraft in the United States must undergo a routine annual inspection or every one hundred flight hours to verify the aircraft's airworthiness as stipulated by Federal Aviation Administration guidelines. This periodic maintenance strategy is called time-based maintenance (TBM). For commercial jets, airlines also schedule heavy maintenance checks at longer intervals, which entails some disassembly of the aircraft and meticulous inspection of all its components and structures. Performing this heavy maintenance is expensive and requires significant time out of service.

Additionally, the increasing adoption of advanced composites for aircraft structures can make the inspection process even more complex and costly as composite materials exhibit different failure mechanisms than traditional metallic materials.

A potential course to alleviate the expense, equipment downtime, and workload of heavy maintenance checks is to incorporate condition-based maintenance (CBM) strategies in tandem with TBM. In CBM, targeted, proactive maintenance is performed informed by data gathered from continuously monitoring the state of the system for precursors to failure [1–3]. Effective employment of CBM requires real-time material state awareness (MSA). MSA involves understanding the material properties, damage processes, and operational environment of a system while continuously monitoring its current state to predict its future state and remaining lifetime [4]. Real-time condition monitoring can be achieved through embedded nondestructive evaluation (NDE) sensor networks, but the implementation of such networks entails numerous challenges, such as the feasibility of sensor installation into the structure, optimization of the sensor configuration, and long term sensor reliability. One way to circumvent these challenges is to make components of self-sensing materials.

Self-sensing materials are able to transduce a quantity of interest through a measurable signal [5]. In essence, the structure itself functions as a sensor. Piezoresistive materials are a type self-sensing material that exhibit a change in electrical conductivity when subject to mechanical strain. This innate ability of piezoresistive materials to transduce the effects of strains through conductivity changes has motivated research employing piezoresistive materials for condition monitoring applications. For instance, electrical impedance tomography (EIT) is a technique that images a spatially continuous, internal conductivity distribution of a piezoresistive material. EIT has been employed to detect and localize damage in composite components [6–15], sense damage and strain in polymer thin films [16, 17], and monitor crack propagation in cement [18–23]. However, beyond serving as a damage detection and localization technique, the conductivity change data obtained by EIT does not provide further insight into the mechanical state of the material. In other words, conductivity change data does not directly translate into stresses, strains, and displacements, values that are more informative for engineers performing stress and failure analysis. To bridge this gap, Tallman and Wang [24] formulated the self-sensing inverse problem (SSIP), a mathematical method that recovers the strain state giving rise to an observed conductivity distribution.

Recovery of the strain and displacement fields of piezoresistive materials under load via the SSIP has been demonstrated both computationally and experimentally. Tallman and Wang [24] first demonstrated the SSIP computationally by recovering the displacement field of a simulated unit cube subject to uniform, compression, shear, and combined tension and shear stress on one of its faces with reasonable accuracy. The SSIP was later demonstrated experimentally when Tallman et al. [25, 26] indented a carbon nanofiber (CNF)-modified polyurethane specimen with spherical marbles and measured the resulting conductivity change distribution with EIT. Using the SSIP, the displacement field of the deformed specimen was reconstructed and matched finite element simulation with good accuracy. Hassan and Tallman [27] incorporated a genetic algorithm into the SSIP and experimentally validated this new formulation on a CNF-modified epoxy through-hole tension test specimen. The specimen was loaded under displacement control, and the conductivity distribution was imaged by EIT at several levels of tension. The displacement field and first principal strain reconstructed by the SSIP demonstrated good agreement with finite element prediction and digital image correlation (DIC) results.

While self-sensing materials can potentially reduce the need for complex sensor networks, MSA often requires monitoring a diverse set of metrics, which could include material strain, temperature, and vibrational response. Currently, no single sensor, evaluation technique, or self-sensing material can fully capture the mechanical state of a structure; thus, sensor networks composed of a variety of sensor types are still necessary. The challenge then arises in effectively integrating the heterogeneous

sensor data to extract useful information. In general, the concept of synergistically combining data from multiple sensors to enhance data reliability and obtain a more accurate understanding of a system than could be achieved by a single sensor alone is known as sensor data fusion (SDF) [28]. SDF is a diverse research topic with roots in military applications and data processing [29–32]. Examples of SDF most relevant to MSA and CBM come from the field of NDE [33–43]. For instance, Zonta et al. [44] improved the accuracy of the load estimation on the stay cables of a bridge in Italy by using probabilistic methods to fuse fiber-optic strain sensor, elasto-magnetic load sensor, and temperature data. Heideklang and Shoukouhi [45] demonstrated increased reliability of detecting near-surface cracks in steel by fusing eddy current, magnetic flux leakage, and thermography data over the use of any one technique alone. As a final example, Pashoutani et al. [46] enhanced defect detection in a reinforced concrete bridge deck by fusing spatial vertical electrical impedance data and ground-penetrating radar maps. The resulting data revealed cracks and defects not clearly visible when analyzing the data separately.

From the preceding discussion, it is evident that the SSIP has potential to aid in failure prognosis and precise monitoring of the mechanical state of piezoresistive materials. However, current SSIP research has not yet progressed beyond computational validation on simple geometries and experimental demonstration using basic test specimen. Furthermore, the SSIP is ill-posed and underdetermined. Thus far, research has sought to improve convergence by implementing metaheuristic global search algorithms [27, 47, 48]. In this work, we explore another route: employing SDF methods to improve the accuracy and reliability of the SSIP. Considering that the SSIP solely relies on conductivity imaging data for its predictions, we envision that fusing complementary data from a small number of discrete sensors, such as strain gauges, with the conductivity data could guide the SSIP toward reconstructing the physically correct strain and displacement field. Thus, we herein develop computational techniques to fuse conductivity imaging data, obtained via a method like EIT, with discrete displacement and strain data. We then computationally demonstrate the SSIP displacement field recovery enhanced with these SDF techniques on more realistic geometries representing aircraft components subject to simulated operational loads. Therefore, this manuscript makes **two novel contributions:** First, the computational form of the SDF-enhanced SSIP is derived. And second, this formulation is computationally validated on a variety of geometries of representative complexity using an experimentally validated piezoresistivity model.

The remainder of this article is organized as follows. First, we present the mathematical formulation of the SSIP. Next, we formulate two computational SDF methods, one involving the fusion of electrical imaging data with displacement data, and the other the fusion of electrical imaging data with strain data. Then, we describe the computational experiments designed to test the SDF methods. This is followed by a discussion of the validation study. Finally, we close this article with a summary, conclusions, and possible avenues for future work.

2. The Self-Sensing Inverse Problem

The SSIP recovers the strain distribution of a piezoresistive material by minimizing the difference between an observed conductivity distribution, imaged for instance using EIT, and one predicted by a piezoresistivity model. Recovering an accurate strain state can be challenging because the SSIP is innately ill-posed, meaning the recovered strain state is highly sensitive to noise and outliers in the conductivity data. The SSIP is also an underdetermined problem because it possesses more degrees of freedom than constraining equations (i.e., strain is a tensor field, whereas isotropic conductivity is a scalar field). Thus, the solution recovered is not unique. Overall, these shortcomings either cause the SSIP to fail to converge or arrive at solutions without physical meaning. To begin, we first discuss the piezoresistivity model used to obtain the model predicted conductivity.

2.1. Piezoresistivity Model

In this work, we use the analytical piezoresistivity model developed by Koo and Tallman [49]. This model predicts a resistivity change for a given strain tensor. The SSIP ultimately seeks to invert this model and obtain the underlying strain state for a given resistivity distribution (e.g., as imaged via EIT). Shown in equation (1) below, $\Delta\rho$ is the resistivity change in ohm-meters ($\Omega \cdot \mathrm{m}$), the terms denoted with ε are components of the infinitesimal strain tensor, and κ, Π_1, and Π_2 are piezoresistive constants. The values of these constants are presented in Table 1. At a high level, the model is a curve fit of experimental data relating strain to resistivity change. Readers interested in the formulation of the model and derivation of the piezoresistive constants are referred to [49].

$$\begin{aligned}\Delta\rho = \kappa(\varepsilon_{11}+\varepsilon_{22}+\varepsilon_{33}) + (\Pi_1+\Pi_2)(\varepsilon_{11}^2+\varepsilon_{22}^2+\varepsilon_{33}^2) \\ + 2\Pi_1(\varepsilon_{11}\varepsilon_{22}+\varepsilon_{33}\varepsilon_{11}+\varepsilon_{22}\varepsilon_{33}) + 2\Pi_2(\varepsilon_{12}^2+\varepsilon_{31}^2+\varepsilon_{23}^2) \quad (1)\end{aligned}$$

This piezoresistivity model was selected for the following reasons. First, this model has been extensively experimentally validated [49]. Second, this model predicts resistivity changes from general deformations (i.e., beyond simple cases of, for example, uniaxial stress), making it applicable to complex load cases and strain states at macroscales, unlike the majority of piezoresistivity models which are limited to the microscale. Lastly, analytical piezoresistivity models are readily incorporated into computational inverse problems, such as herein presented. It is important to note that this model was developed assuming linear elastic material behavior and infinitesimal strains.

2.2. Mathematical Formulation

Before proceeding, note that it had been stated that the SSIP reconstructs the strain state from electrical conductivity data. However, electrical resistivity is hereon used instead because the piezoresistivity model is in terms of resistivity. Additionally, although we presume the use of EIT to obtain the experimental resistivity distribution, EIT is not the crux of this research. For a comprehensive treatment of EIT, interested readers are directed to EIT focused work [17, 18, 50]. It is instead assumed that the resistivity distribution is known.

The SSIP is expressed as the minimization problem shown in equation (2), where ρ is the experimentally observed resistivity distribution, $f(\varepsilon_{ij})$ is the model-predicted resistivity distribution (i.e., equation (1)), and ε_{ij}^* is the spatially varying strain that satisfies the minimization.

$$\varepsilon_{ij}^* = \underset{\varepsilon_{ij}}{\arg\min}(\|\rho - f(\varepsilon_{ij})\|^2) \quad (2)$$

Note that the ρ in equation (2) is an absolute resistivity, but the piezoresistivity model predicts a resistivity change. Thus, $f(\varepsilon_{ij})$ is defined as $f(\varepsilon_{ij}) = \Delta\rho + \rho_0$, where ρ_0 is a baseline resistivity. Next, $f(\varepsilon_{ij})$ is linearized via a Taylor series expansion about an initial estimate of the strain state, ε_{ij}^0, as shown in equation (3). Substituting equation (3) back into equation (2) yields equation (4).

$$f(\varepsilon_{ij}) \cong f(\varepsilon_{ij}^0) + \frac{\partial f(\varepsilon_{ij}^0)}{\partial \varepsilon_{ij}}(\varepsilon_{ij} - \varepsilon_{ij}^0) \quad (3)$$

$$\varepsilon_{ij}^* = \underset{\varepsilon_{ij}}{\arg\min}\left(\left\|\rho - f(\varepsilon_{ij}^0) - \frac{\partial f(\varepsilon_{ij}^0)}{\partial \varepsilon_{ij}}(\varepsilon_{ij} - \varepsilon_{ij}^0)\right\|^2\right) \quad (4)$$

By defining the difference between the observed and model determined resistivity as $\delta\rho = \rho - f(\varepsilon_{ij})$ and the difference between the true strain and estimated strain as $\delta\varepsilon_{ij} = \varepsilon_{ij} - \varepsilon^0_{ij}$, we arrive at equation (5).

$$\varepsilon^*_{ij} = \arg\min_{\varepsilon_{ij}} \left(\left\| \delta\rho - \frac{\partial f(\varepsilon^0_{ij})}{\partial \varepsilon_{ij}} \delta\varepsilon_{ij} \right\|^2 \right) \tag{5}$$

The next step is to modify equation (5) to be applicable to a finite element mesh. This is done because EIT ordinarily images the resistivity distribution of a domain that is discretized by a finite element mesh, with each mesh element assigned a constant resistivity value. Furthermore, employing the SSIP on non-trivial geometries requires some discretization of the solution space. Thus, we naturally aim to recover the strain state on the same mesh used for resistivity imaging. In this work, the geometries are discretized into meshes of trilinear hexahedral elements. Hexahedral elements are selected because they are commonly used in structural simulations and generally produce more accurate results than linear tetrahedral elements. To begin, we recall the definition of the infinitesimal strain tensor and the finite element forms of displacement, u_i, and the displacement gradient, $\partial u_i/\partial x_j$, given in equations (6), (7), and (8), respectively.

$$\varepsilon_{ij} = \frac{1}{2}\left(\frac{\partial u_i}{\partial x_j} + \frac{\partial u_j}{\partial x_i} \right) \tag{6}$$

$$u_{e,i} = \sum_A N^A d^A_{e,i} \tag{7}$$

$$\frac{\partial u_{e,i}}{\partial x_j} = \sum_A \frac{\partial N^A}{\partial \xi_k} \frac{\partial \xi_k}{\partial x_j} d^A_{e,i} \tag{8}$$

In the above equations, $u_{e,i}$ is the displacement in the i-direction of the eth element, N^A is the trilinear finite element interpolation function for the Ath node of a hexahedral element, and $d^A_{e,i}$ is the displacement in the i-direction of the Ath node of the eth element. The summation $\sum_A(\cdot)$ runs from one to eight for hexahedral elements. Summation is implied over repeated indices.

The use of trilinear hexahedral elements conflicts with the treatment of resistivity as a constant value for each element. This is because the strains are not constant throughout a hexahedral element. This results in a dimensional mismatch between the terms being subtracted in equation (5). To remedy this, a strain tensor with constant components can be obtained for each element by computing the volumetric average of $\partial u_{e,i}/\partial x_j$ as shown in equation (9).

$$\frac{\partial \bar{u}_{e,i}}{\partial x_j} = \frac{\int_{v_e} \sum_A \frac{\partial N^A}{\partial \xi_k} \frac{\partial \xi_k}{\partial x_j} d^A_{e,i} \, \mathrm{d}v_e}{v_e} = \sum_A \frac{\int_{v_e} \frac{\partial N^A}{\partial \xi_k} \frac{\partial \xi_k}{\partial x_j} \, \mathrm{d}v_e}{v_e} d^A_{e,i} = \sum_A \frac{\partial \bar{N}^A}{\partial x_j} d^A_{e,i} \tag{9}$$

The bar accent signifies a volumetric average, and v_e is the volume of the eth element. The third term of the equality exercises the sum rule of integration, and $d^A_{e,i}$ is moved outside of the integral because the nodal displacements are constant. By substituting $\partial \bar{u}_{e,i}/\partial x_j$ for $\partial u_{e,i}/\partial x_j$, we are able to recast equation (5) as equation (10) for a single hexahedral element.

$$\varepsilon^*_{e,ij} = \arg\min_{\varepsilon_{ij}} \left(\left\| \delta\rho_e - \frac{\partial f(\varepsilon^0_{ij})}{\partial \varepsilon_{ij}} \sum_A \frac{\partial \bar{N}^A}{\partial x_j} \delta d^A_{e,i} \right\|^2 \right) \tag{10}$$

Equation (10) can be re-expressed using linear algebra. The process begins by modifying the term with the summation as shown by equation (11). First, $\partial f(\varepsilon_{ij}^0)/\partial\varepsilon_{ij}$ is moved inside the summation. Then, the explicit summation is replaced with the multiplication of a row and column vector for the eth element.

$$\frac{\partial f(\varepsilon_{ij}^0)}{\partial\varepsilon_{ij}}\sum_A \frac{\partial \bar{N}^A}{\partial x_j}\delta d_{e,i}^A = \sum_A \frac{\partial f(\varepsilon_{ij}^0)}{\partial\varepsilon_{ij}}\frac{\partial \bar{N}^A}{\partial x_j}\delta d_{e,i}^A = \begin{bmatrix} g_{e1}^1 & g_{e2}^1 & \dots & g_{e3}^8 \end{bmatrix} \begin{bmatrix} \delta d_{e1}^1 \\ \delta d_{e2}^1 \\ \vdots \\ \delta d_{e3}^8 \end{bmatrix} \tag{11}$$

The elemental $\boldsymbol{g_e}$ and $\delta\boldsymbol{d_e}$ vectors are assembled into a global matrix, $\boldsymbol{G}$, and global nodal displacement increment vector, $\delta\boldsymbol{d}$, such that the element level contractions are preserved. Equation (12) expresses the minimization for the entire mesh, where $\delta\boldsymbol{\rho}$ is now a global vector of the difference between observed and model resistivity. Note that we now seek a global displacement vector, $\boldsymbol{d^*}$, giving rise to an observed resistivity change. The transition from ε_{ij}^* to $\boldsymbol{d^*}$ is a consequence of the infinitesimal strain tensor being expressed in terms of nodal displacements as part of the finite element formulation.

$$\boldsymbol{d}^* = \arg\min_d(\|\delta\boldsymbol{\rho} - \boldsymbol{G}\delta\boldsymbol{d}\|^2) \tag{12}$$

Solving for $\boldsymbol{d^*}$ is an iterative process. To begin, we first set the initial estimate of the global displacement vector as $\boldsymbol{d}^0 = \boldsymbol{0}$ because we assume no prior knowledge of the state of the material. $\boldsymbol{d}^0$ is used to calculate the initial ε_{ij}^0, $f(\varepsilon_{ij}^0)$, and $\partial f(\varepsilon_{ij}^0)/\partial\varepsilon_{ij}$, for each element. The global $\boldsymbol{G}$ matrix and $\delta\boldsymbol{\rho}$ vector are then assembled. At this point, any columns of $\boldsymbol{G}$ corresponding to nodal degrees of freedom subject to displacement boundary conditions are removed, similar to a standard finite element simulation.

Next, we calculate $\delta\boldsymbol{d}$. To do so, we first recognize that recovering three independent components of displacement from a scalar resistivity is an underdetermined problem. Thus, we calculate $\delta\boldsymbol{d}$ by employing a least squares-like method with regularization shown in equation (13). Regularization aims to stabilize the inverse problem by imposing an assumed condition or prior knowledge of the solution space. In the equation below, $\boldsymbol{L}$ is the discrete Laplacian used for regularization, and α is the scalar regularization parameter. $\boldsymbol{L}$ is chosen because it promotes a smoothly varying solution space, which is a reasonable assumption for a displacement field. After $\delta\boldsymbol{d}$ is calculated, $\boldsymbol{d}$ is updated as $\boldsymbol{d}^{n+1} = \boldsymbol{d}^n + \delta\boldsymbol{d}$. ε_{ij}^n, $f(\varepsilon_{ij}^n)$, and $\partial f(\varepsilon_{ij}^n)/\partial\varepsilon_{ij}$ are recalculated to proceed with the next iteration. Iterations continue until the minimization in equation (12) is satisfied.

$$\delta\boldsymbol{d} = (\boldsymbol{G}^T\boldsymbol{G} + \alpha^2\boldsymbol{L}^T\boldsymbol{L})^{-1}\boldsymbol{G}^T\delta\boldsymbol{\rho} \tag{13}$$

3. Sensor Data Fusion Techniques

Herein, we explore fusing resistivity data with displacement and strain data. That is, in addition to the resistivity distribution from EIT, a few points within the domain will possess either displacement or strain sensors. Displacement data is a logical choice because the SSIP already directly solves for a displacement field. Strain data is also considered because strain gauges are commonly used in structural applications. When integrating heterogeneous sensor data, a common reference frame must be established to ensure that the data from each sensor are assigned to the correct physical points on the specimen, known as data registration. The SSIP reconstructs the displacements and strains on the same finite element mesh the resistivity data is imaged. Therefore,

the finite element mesh conveniently functions as the common reference frame because all three data types are already defined mesh properties. Resistivity and strain are elemental properties, and displacement is a nodal property. After the physical sensor locations on the specimen are selected, to incorporate displacement sensor data, the mesh node at the physical sensor location is designated as a displacement sensor (DS), at which the nodal displacements will be known. To incorporate strain data, the mesh element at the sensor location is designated as a strain sensor (SS) at which the elemental strains will be known. In the following sections, we develop methods for resistivity-displacement and resistivity-strain SDF.

3.1. Fusion of Resistivity and Displacement Data

The resistivity-displacement SDF process begins with replacing all columns of $\boldsymbol{G}$ associated with DS nodes with zero column vectors. This is done for two reasons. First, in a matrix equation, a zero column in the matrix indicates a free variable. Thus, as a result of the column replacement, the DS nodes no longer constrain the least squares solution and can be assigned any value. The second reason is to preserve the dimensions of $\boldsymbol{L}$. When a column of $\boldsymbol{G}$ is removed, the corresponding rows and columns of $\boldsymbol{L}$ must also be removed to maintain dimensional compatibility in equation (13). Removal of rows and columns from $\boldsymbol{L}$, however, disconnects the corresponding nodes from the smooth solution space promoted by $\boldsymbol{L}$, which can cause aberrations in the reconstructed displacement field at and near DS nodes.

The SSIP then proceeds normally with the calculation of $\delta\boldsymbol{d}$. Following this, the entries of $\boldsymbol{d}^n$ belonging to DS nodes are replaced with corresponding DS data, overwriting the unconstrained displacement values calculated previously. However, the direct insertion of sensor data into $\boldsymbol{d}^n$ may cause the SSIP to diverge or attain a nonsensical solution. This occurs because the DS data is often much larger than the SSIP predicted displacements, especially during the early iterations. The sharp disparity between DS and SSIP predicted displacements results in the calculation of large elemental strains and, consequently, outlier model predicted resistivity. This outlier resistivity can cause the SSIP to predict erroneous displacements in the following iteration, an error which compounds with each iteration. To overcome this problem, displacement data are incorporated using the function defined by equation (14).

$$\boldsymbol{d}^n_{DS} = \Psi(n)\boldsymbol{d}_{known} \tag{14}$$

Equation (14) reduces the discrepancy in the displacement values among DS and non-DS nodes to maintain the stability of the SSIP by ramping the displacement data. $\boldsymbol{d}^n_{DS}$ is the subset of $\boldsymbol{d}^n$ belonging to DS nodes at the nth iteration, $\boldsymbol{d}_{known}$ is the measured displacement data, and $\Psi(n)$ is a ramping function. $\Psi(n)$ is selected such that it is a positive, decimal value that approaches one. Herein, we select a piecewise linear function for $\Psi(n)$, shown in equation (15). In essence, 10% of the DS data is added with each iteration such that by the tenth iteration, the full displacement data has been incorporated. While no rigorous technique was used to select the slope of the linear ramping function, it was observed that a gentler slope reduced the risk of SSIP divergence. Optimal selection of the rate of DS data ramping involves a tradeoff between SSIP stability and number of iterations required to converge to a solution.

$$\Psi(n) = \begin{cases} \frac{n}{10}, & n < 10 \\ 1, & n \geq 10 \end{cases} \tag{15}$$

3.2. Fusion of Resistivity and Strain Data

The resistivity-strain SDF technique is predicated on the idea of enforcing additional constraints on the displacement field solution by incorporating strain-displacement relations. This is accom-

plished by adapting and incorporating a technique known as the inverse Finite Element Method (iFEM). Developed by Tessler et al. [51–53], iFEM is a computational method which aims to reconstruct the displacement field of a finite element discretized structure from a set of discrete strain measurements by minimizing a least squares functional. Strains are treated as an elemental mesh property, and measured strains are assigned to the mesh element on which the sensor is located. A key challenge for iFEM is the availability of measured strain data. In practice, strain sensor networks are often sparse, and each sensor can only measure particular strain components. One solution to this problem is to 'pre-extrapolate' the strains for mesh elements without strain data. In other words, the strains for elements without strain data can be estimated, for instance, using statistical [54] or physics-based [55] methods.

Because iFEM possesses a similar objective and mathematical formulation to the SSIP, we integrate iFEM with the SSIP to fuse resistivity and strain data. The following is the derivation of iFEM equations beginning with the error functional. The derivation generally adheres to previous work done in iFEM with modifications to accommodate the SSIP parameters. To begin, we define the error functional in equation (16) for a single mesh element. Below, $d_{e,i}^A$ is the nodal displacement vector, $\varepsilon_e(d_{e,i}^A)$ are the elemental strains predicted via a model (i.e. strain displacement relations), and $\bar{\varepsilon}_e$ are the measured strains. The strains, ε, are defined as a column vector of the six independent strain components given in equation (17). W_e is a 6×6 diagonal matrix containing constant weight coefficients corresponding to each strain component. A large weight is assigned to strain components with measured data, and a smaller weight is assigned to strains without measured data. The selection of values for weight coefficients is discussed in Section 5.2.

$$\Phi_e(d_{e,i}^A) = W_e \|\varepsilon_e(d_{e,i}^A) - \bar{\varepsilon}_e\|^2 \tag{16}$$

$$\varepsilon = \begin{bmatrix} \varepsilon_{11} & \varepsilon_{22} & \varepsilon_{33} & \varepsilon_{12} & \varepsilon_{13} & \varepsilon_{23} \end{bmatrix}^T \tag{17}$$

Next, we express $\varepsilon_e(d_{e,i}^A)$ using linear algebra. To do so, we construct an elemental strain-displacement matrix, B_e, as shown in equation (18), which maps the element nodal displacements to the elemental strain components in equation (17). Thus, $\varepsilon_e(d_{e,i}^A)$ is now explicitly expressed as the matrix equation in (19).

$$B_e = \begin{bmatrix} \frac{\partial N^1}{\partial x_1} & 0 & 0 & \frac{\partial N^2}{\partial x_1} & 0 & 0 & \cdots & \frac{\partial N^8}{\partial x_1} & 0 & 0 \\ 0 & \frac{\partial N^1}{\partial x_2} & 0 & 0 & \frac{\partial N^2}{\partial x_2} & 0 & \cdots & 0 & \frac{\partial N^8}{\partial x_1} & 0 \\ 0 & 0 & \frac{\partial N^1}{\partial x_3} & 0 & 0 & \frac{\partial N^2}{\partial x_3} & \cdots & 0 & 0 & \frac{\partial N^8}{\partial x_3} \\ \frac{1}{2}\frac{\partial N^1}{\partial x_2} & \frac{1}{2}\frac{\partial N^1}{\partial x_1} & 0 & \frac{1}{2}\frac{\partial N^2}{\partial x_2} & \frac{1}{2}\frac{\partial N^2}{\partial x_1} & 0 & \cdots & \frac{1}{2}\frac{\partial N^8}{\partial x_2} & \frac{1}{2}\frac{\partial N^8}{\partial x_1} & 0 \\ \frac{1}{2}\frac{\partial N^1}{\partial x_3} & 0 & \frac{1}{2}\frac{\partial N^1}{\partial x_1} & \frac{1}{2}\frac{\partial N^2}{\partial x_3} & 0 & \frac{1}{2}\frac{\partial N^2}{\partial x_1} & \cdots & \frac{1}{2}\frac{\partial N^8}{\partial x_3} & 0 & \frac{1}{2}\frac{\partial N^8}{\partial x_1} \\ 0 & \frac{1}{2}\frac{\partial N^1}{\partial x_3} & \frac{1}{2}\frac{\partial N^1}{\partial x_2} & 0 & \frac{1}{2}\frac{\partial N^2}{\partial x_3} & \frac{1}{2}\frac{\partial N^2}{\partial x_2} & \cdots & 0 & \frac{1}{2}\frac{\partial N^8}{\partial x_3} & \frac{1}{2}\frac{\partial N^8}{\partial x_2} \end{bmatrix} \tag{18}$$

$$\varepsilon_e(d_{e,i}^A) = B_e d_{e,i}^A \tag{19}$$

Substituting equation (19) into (16) yields the first term of equation (20). Here, the superscript A and subscript i are omitted for notational clarity. Then, the 2-norm is converted into its equivalent integral form. By expanding the integrand and consolidating terms, we obtain the final term of equation (20). Below, K_e is the elemental iFEM stiffness matrix and f_e is the elemental iFEM

forcing vector.

$$\begin{aligned}\Phi_e(d_{e,i}^A) &= W_e\|B_e d_e - \bar{\varepsilon}_e\|^2 \\ &= W_e \int_V [B_e d_e - \bar{\varepsilon}_e]^2 dV \\ &= \int_V (d_e^T B_e^T W_e B_e d_e - 2 d_e^T B_e^T W_e \bar{\varepsilon}_e + \bar{\varepsilon}_e^T W_e \bar{\varepsilon}_e) dV \\ &= d_e^T \left[\int_V B_e^T W_e B_e dV\right] d_e - 2 d_e^T \left[\int_V B_e^T W_e \bar{\varepsilon}_e dV\right] + \int_V \bar{\varepsilon}_e^T W_e \bar{\varepsilon}_e dV \\ &= d_e^T K_e d_e - 2 d_e^T f_e + c\end{aligned} \tag{20}$$

Next, the error functional is minimized by taking the variation of Φ_e with respect to $d_{e,i}^A$ and setting it equal to zero, as shown in equation (21). The elemental K_e matrix and f_e vectors are then assembled into a global $\boldsymbol{K}$ matrix and $\boldsymbol{F}$ vector, resulting in equation (22).

$$\delta\Phi_e = K_e d_{e,i}^A - f_e = 0 \tag{21}$$

$$\boldsymbol{K}\boldsymbol{d} - \boldsymbol{F} = 0 \tag{22}$$

Equation (22) contains the set of all iFEM equations. The goal is to combine equation (22) with the existing SSIP equations in equation (12). To proceed, $\boldsymbol{d}$ in equation (22) is converted to $\delta\boldsymbol{d}$. In other words, iFEM is modified to predict a displacement increment instead of displacement to be compatible with the SSIP. As a result of this change, $\bar{\varepsilon}_e$ in f_e is also converted to a strain increment, $\delta\bar{\varepsilon}_e$, where $\delta\bar{\varepsilon}_e$ represents the difference between the true strain and the model predicted strains. For SS elements, $\delta\bar{\varepsilon}_e = \bar{\varepsilon}_e - \varepsilon_{e,ij}^n$, where $\varepsilon_{e,ij}^n$ is the SSIP-predicted strain tensor for the eth element at the nth iteration. For elements without strain data, we devise the following strain pre-extrapolation method. Prior to each iteration, $\delta\boldsymbol{d}$ is calculated using equation (13), hereon denoted as $\delta\boldsymbol{d}^X$. $\delta\boldsymbol{d}^X$ is used to calculate a strain increment tensor for every non-SS mesh element $\delta\boldsymbol{\varepsilon}_{e,ij}^X$, and $\delta\bar{\varepsilon}_e = \delta\varepsilon_{e,ij}^X$. To clarify, $\delta\bar{\varepsilon}_e$ is a $[6 \times 1]$ vector while $\delta\varepsilon_{e,ij}^X$ and $\delta\varepsilon_{e,ij}^n$ are second order tensors. By equating the vector to the tensor, the intent is to convey that the strain components of the vector are set equal to the corresponding strain components in the tensor. Together, these modifications produce equation (23). $\boldsymbol{K}$ matrix and $\delta\boldsymbol{F}$ vector are then directly concatenated to the SSIP $\boldsymbol{G}$ matrix and $\delta\boldsymbol{\rho}$ vector, respectively, resulting in equation (24).

$$\boldsymbol{K}\delta\boldsymbol{d} - \delta\boldsymbol{F} = 0 \tag{23}$$

$$\boldsymbol{d}^* = \arg\min_d \left(\left\| \begin{bmatrix} \delta\boldsymbol{\rho} \\ \delta\boldsymbol{F} \end{bmatrix} - \begin{bmatrix} \boldsymbol{G} \\ \boldsymbol{K} \end{bmatrix} \delta\boldsymbol{d} \right\|^2 \right) \tag{24}$$

The iterative process to recover $\boldsymbol{d}^*$ remains mostly unchanged from the original SSIP except that regularization via $\boldsymbol{L}$ is no longer required to solve for $\delta\boldsymbol{d}$. This is because the strain-displacement relations in $\boldsymbol{K}$ provide some degree of regularization. The MATLAB function '*lsqlin*' is used to solve equation (24) for $\delta\boldsymbol{d}$.

4. Computational Experiment Design

4.1. Geometries, Load Cases, and Set Up

Because SSIP research to date has focused on simple geometries, for this study, three shapes representing aircraft components were selected for investigation, shown in Figure 1. From left to right, the shapes are a T-shaped mounting bracket, the skin of an aircraft wing, and a section of an aircraft wing spar, hereon referred to as the mounting bracket, airfoil, and wing spar, respectively. These shapes were selected because they represent components that could be of interest for MSA and CBM. To clarify, the shapes modeled and loads simulated are not derived from actual part drawings or rigorous engineering analysis—the intent is solely to demonstrate that the SSIP can be employed for more practical geometries.

Each shape was subject to a load roughly simulating a real world operational load. The load case and resulting deformation for each geometry are illustrated in Figure 1. The magnitude of the loads were selected such that the resulting strains fell within the bounds which the piezoresistivity model is known to be accurate. Specifically, no axial strains could exceed $\pm 6.0 \times 10^{-3}$, and no shear strains could exceed $\pm 1.5 \times 10^{-2}$ [49].

The mounting bracket is a fixed-free cantilever, with the rear face of the flange fixed and the web free. In practical application, the rear face would be bolted to a rigid surface, and the web would serve as a mounting plate for a load bearing member to attach to. The load case considered simulates a load bearing member mounted to the web at an 45° counter-clockwise angle from the $+y$-axis under tension. Since tension along the member transfers to the rigid surface through the mounting bracket via shear on the web, a 155 kPa uniform shear stress is applied to both sides of the web.

The airfoil is an open-ended hollow shell with a thickness of 2.54 mm. Both ends of the airfoil are fixed, and the trailing edge is truncated at the 80% chord position. The selected shell thickness and omission of the trailing edge avoids potential meshing complications that may arise from discretizing a thin shell and a sharp edge using hexahedral elements. The chosen load case roughly simulates the net pressure distribution on the wing at 5° angle of attack and 45 m/s airspeed at sea-level. The pressure distribution was calculated by extending a two-dimensional pressure distribution predicted by *XFOIL* [56] along the span of the wing, neglecting the three-dimensional effects of a finite wing. Since the focus of this research is the SSIP and SDF, the approximations of the aerodynamic loading and wing geometry are deemed acceptable.

The wing spar is also a fixed-free cantilever. The fixed end would be the root of the wing spar connected to the aircraft fuselage, and the free end would be toward the wing tip. During maneuvering flight, aerodynamic loads on an aircraft wing can induce twist—a rotation of the wing about its longitudinal axis. To simulate this for the wing spar, the surfaces of the spar caps are subject to a 10 kPa uniform shear stress in opposite directions along the z-axis.

To prepare the shapes for the computational experiments, each was discretized into two finite element meshes, one coarse mesh and one fine. The finite element displacement solution and resistivity data will first be simulated on the fine mesh, after which the resistivity data is averaged onto the coarse mesh on which the SSIP is performed. All shapes were assigned the mechanical and piezoresistive properties of 1 wt.% CNF/epoxy. While CNF/epoxy is obviously not a realistic material for structural components, it was selected because an experimentally validated piezoresistivity model for the material already exists [49]. It was also assumed that the undeformed material has a baseline uniform resistivity distribution of 75,000 $\Omega \cdot$ m, a value derived from experimental characterization [57]. The elastic properties and piezoresistivity model constants used are displayed in Table 1.

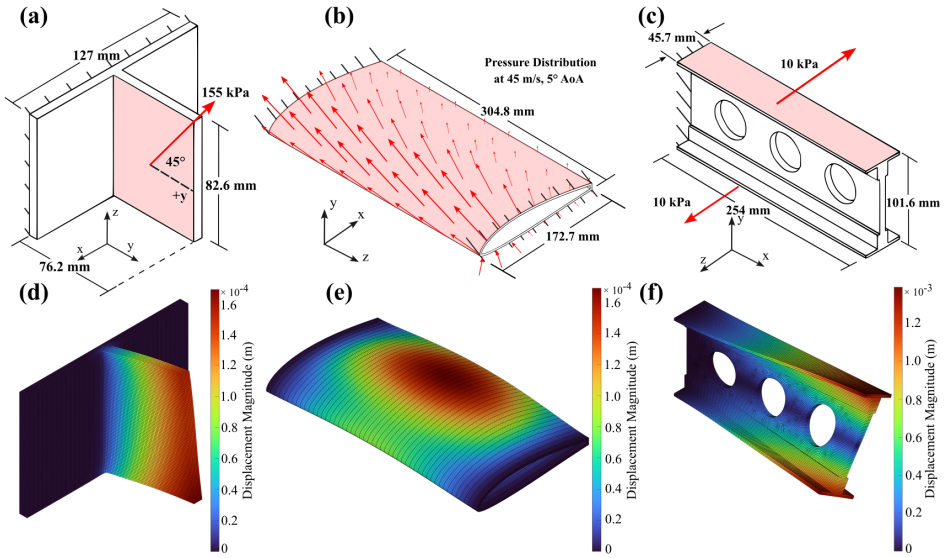

Figure 1: Top row: illustration of the load case for the (a) mounting bracket, (b) wing spar, and (c) airfoil. Bottom row: scaled deformation resulting from the load calculated from finite element analysis.

Table 1: Elastic properties and piezoresistivity model constants used to define 1 wt.% CNF/epoxy.

Mechanical Properties	
E	2.711 GPa
ν	0.351
Piezoresistivity Model Constants	
κ	4.10 $\times 10^{6}$ $\Omega \cdot$ m
Π_1	-1.50 $\times 10^{8}$ $\Omega \cdot$ m
Π_2	5.15 $\times 10^{5}$ $\Omega \cdot$ m
ρ_0	75,000 $\Omega \cdot$ m

After mesh generation, sensor locations were selected on the surface of each shape. In total, 50, 78, and 85 potential sensor locations were identified for the mounting bracket, wing spar, and airfoil, respectively, shown in Figure 2. Not all identified sensor locations are necessarily used in a given computational experiment; rather, they represent the maximum number sensor configuration that was considered for each shape. The locations were selected to be as uniformly spaced as possible across the entire surface of the shape because we attempt to recover the global displacement field. While efficient sensor placement is an extremely important consideration when designing a sensor network, optimizing sensor location falls outside the scope of this research.

At the identified sensor locations, the corresponding node and element from the coarse mesh of each shape can be selected to act as a DS and SS, respectively. The nodal displacements and elemental strains from the fine mesh finite element solution were extracted to serve as sensor data for the DS and SS. In this work, all three components of displacement were known at a DS node. In real world applications, displacements can be measured using experimental methods such as DIC or hardware such as discrete displacement gauges. Although a sensor measuring three-dimensional displacements does not readily exist, we proceed with this assumption to keep the implementation of displacement SDF simple for this computational exploration. For SS elements, a more realistic approach was taken because strain gauges are a common sensor. At each SS, the

in-plane principal and shear strains relative to the surface which the SS resides will be known, replicating the functionality of a strain gauge rosette.

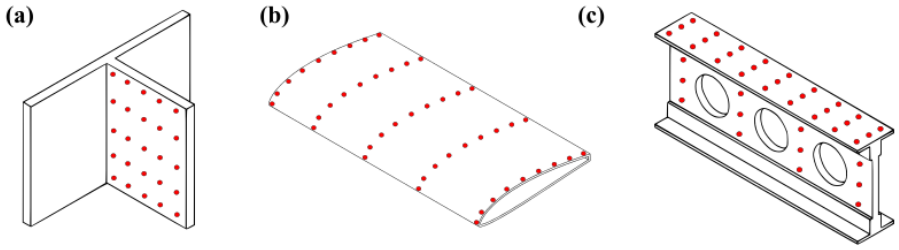

Figure 2: All possible sensor locations for the (a) mounting bracket, (b) airfoil, and (c) wing spar.

4.2. Computational Experiments and Procedures

Each computational experiment followed the procedure illustrated by the flowchart in Figure 3. First, the nodal displacement field solution and elemental strains were calculated on the fine mesh using standard finite element analysis. Next, the simulated resistivity data were generated on the same fine mesh by plugging in the elemental strains into equation (1). Then, the fine mesh resistivity data were averaged onto the coarse mesh. To better represent experimental data, Gaussian white noise was then added to the coarse mesh resistivity data. Two meshes were used to prevent an 'inverse crime' [50] (i.e., the SSIP should not have an exact solution available to it, as would be the case if the same mesh is used to both simulate data and reconstruct displacements). Finally, the SSIP attempted to recover the displacement field from the noisy coarse mesh resistivity data, supplemented by additional displacement or strain data via SDF. A reconstruction was considered successful if the recovered displacement field on the coarse mesh closely matched the fine mesh solution.

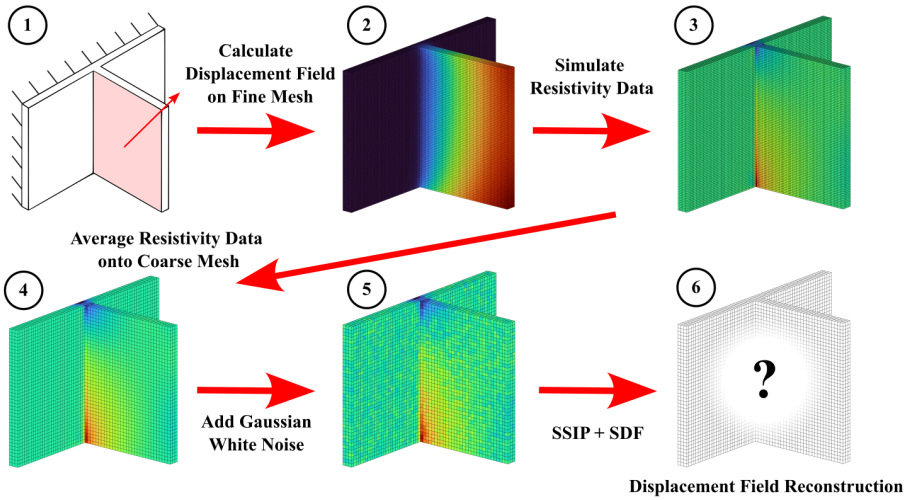

Figure 3: Flowchart depicting the computational experiment procedure.

Two error metrics were plotted to help quantify the quality of the recovered displacement field: the normalized resistivity error, ϵ_ρ^n, and the normalized displacement error, ϵ_d^n, defined by equations (25) and (26), respectively. Equation (25) measures how closely the model predicted resistivity distribution matches the simulated resistivity data, in which $\boldsymbol{\rho}$ and $[\boldsymbol{f}(\varepsilon_{ij})]^n$ are the experimental

and model predicted resistivity distribution, respectively. The norm of the difference between those terms at the nth iteration is normalized by the initial value. Equation (26) measures how closely the displacement field estimate matches the finite element solution. $\boldsymbol{d}_{exact}$ is the displacement field predicted via finite element analysis, and $\boldsymbol{d}^n$ is the reconstructed displacement field at the nth iteration. Both error metrics are expected to converge to zero if the minimization in equation (12) is being satisfied and the SSIP predicted displacement field approaches the true displacement field. It is important to note that in practical application ϵ_d can not be calculated because the user would not have prior knowledge of the exact displacement field. ϵ_d is presented in this study for demonstration purposes only.

$$\epsilon_\rho^n = \frac{\|\boldsymbol{\rho} - [\boldsymbol{f}(\varepsilon_{ij})]^n\|^2}{\|\boldsymbol{\rho} - [\boldsymbol{f}(\varepsilon_{ij})]^0\|^2} \tag{25}$$

$$\epsilon_d^n = \left\| \frac{\boldsymbol{d}_{exact}}{\|\boldsymbol{d}_{exact}\|^2} - \frac{\boldsymbol{d}^n}{\|\boldsymbol{d}_{exact}\|^2} \right\|^2 \tag{26}$$

To evaluate the performance of each SDF method, we performed three computational experiments, each addressing the objectives below.

- Computational Experiment 1: Determine the number of sensors required to improve the accuracy of the SSIP-recovered displacement field.
  The number of sensors providing displacement or strain data was increased from zero to the maximum sensor configuration. The sensors were added in a pattern that maintained symmetry and uniform spacing as closely as possible, but no rigorous method or algorithm was used to design each sensor configuration. The resistivity data used had a 75 dB signal to noise ratio (SNR). To determine the number of sensors required to improve the recovered displacement field, we visually inspected the recovered displacement fields and qualitatively analyzed a plot of the final displacement error, ϵ_d^*, against number of sensors. ϵ_d^* is the value of ϵ_d at the last iteration of the SSIP. These qualitative methods were employed to avoid arbitrarily selecting a threshold value for ϵ_d. The sensor configuration identified here and the corresponding displacement reconstruction serve as the standard configuration and baseline reconstruction for the following experiments.

- Computational Experiment 2: Demonstrate how SDF affects the reliability of the SSIP when resistivity data noise is increased.
  Using the standard sensor configuration identified in Experiment 1, the displacement field was reconstructed from resistivity data with 50, 40, and 30 dB SNR. Visual inspection of the reconstructions and plots ϵ_d were used to make a qualitative judgment on the impact of SDF on SSIP reconstruction reliability.

- Computational Experiment 3: Demonstrate how SDF affects the reliability of the SSIP when there are outlier resistivity data.
  Eight small regions were selected from the coarse mesh of each shape to contain outlier resistivity data. Half of the regions were assigned a resistivity value of 105,000 $\Omega \cdot$ m, and the remaining were assigned 45,000 $\Omega \cdot$ m. These outlier values were selected to be $\pm$30,000 $\Omega \cdot$ m of ρ_0, which is outside the range where the piezoresistivity model is accurate. These outlier data were applied to the resistivity data with 75 dB SNR. The displacement field was recovered the standard sensor configuration.

5. Results and Discussion

This section is divided into two subsections—one dedicated to the results of resistivity-displacement SDF and the other to resistivity-strain SDF. Figure 4 provides the fine mesh displacement field solution for each shape to serve as references for the results below (i.e., the SSIP applied to the coarse meshes seeks to reproduce the displacements of the fine meshes).

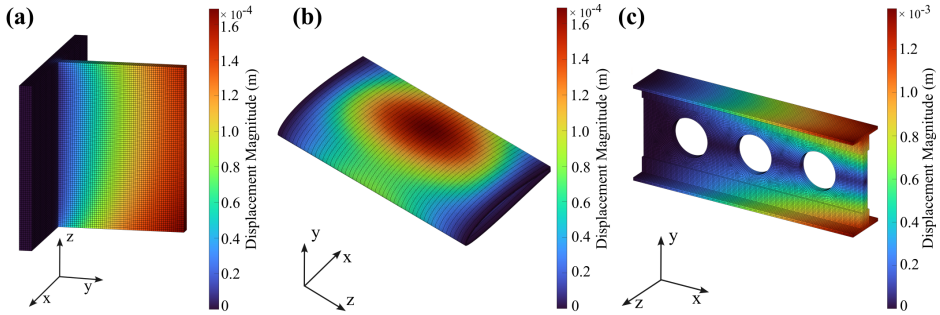

Figure 4: Displacement field solution on the fine mesh for the (a) mounting bracket, (b) airfoil, and (c) wing spar simulated using standard finite element analysis. These are the 'correct' solutions that the SSIP seeks to reproduce. All subsequent displacement maps use the same color scale as the scale in this Figure.

5.1. Resistivity-Displacement Sensor Data Fusion Results

5.1.1. Computational Experiment 1

We first attempted to recover the displacement field of each deformed shape without additional sensor data. The reconstructions are shown in the top-left of Figures 5–7. It is clear that without supplementary data from sensors, the SSIP greatly under-predicts the displacement magnitude and fails to accurately capture the contours of the displacement field for all shapes. The reader may recall that the SSIP was demonstrated both computationally and experimentally to produce relatively good reconstructions in previous works. The reason for the large inaccuracies here could be because of the significantly more complex shapes and load cases being explored.

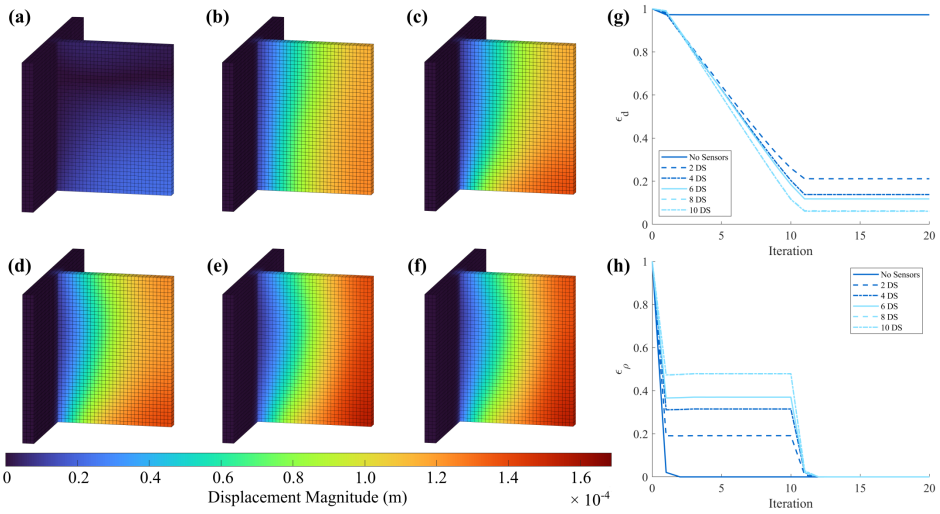

Figure 5: Mounting bracket displacement field reconstructions enhanced with (a) 0, (b) 2, (c) 4, (d) 6, (e) 8, and (f) 10 DS shown along plots of (g) ϵ_d and (h) ϵ_ρ.

With the introduction of DS, the accuracy of the reconstructions improved dramatically. Sensors were added in even number sets to maintain a symmetric configuration. 2 sensors were added at a time up to 18 sensors, after which 8 sensors were added in each new set. For the mounting bracket and wing spar, for each new sensor added, another was placed on the mirror opposite side of the shape. Similarly for the airfoil, every sensor on the upper surface had a corresponding pair at the equivalent span and chord location on the lower surface. From purely visual observation, as the number of DS increased, the displacement reconstruction more closely matched the finite element solution. Using only 2 DS, the displacement magnitude was roughly captured for the mounting bracket and airfoil. With 4 DS, both the displacement magnitude and field contours were reasonably reconstructed for the mounting bracket and wing spar. For the airfoil, 10 DS were needed to recover the field contours. However, new improvements are difficult to visually discern as we continue to add more DS as the reconstructed displacement fields approach the correct solutions.

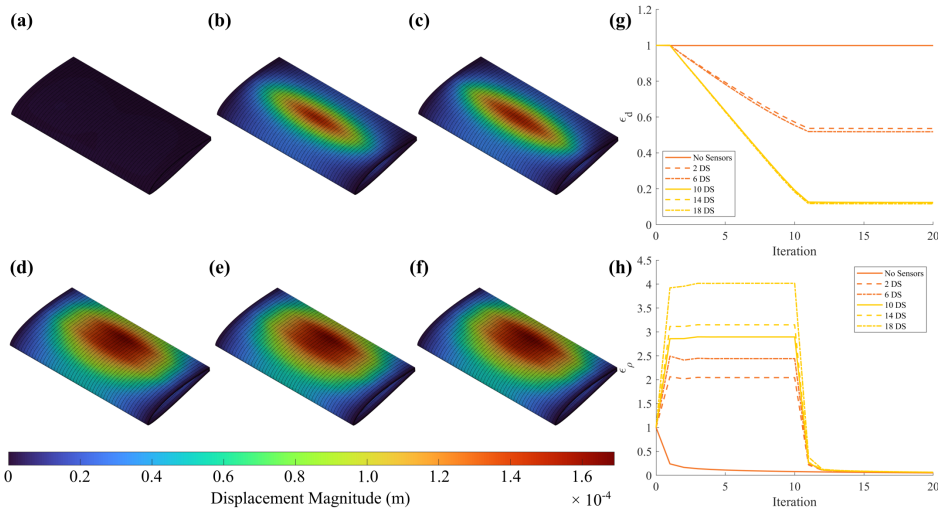

Figure 6: Airfoil displacement field reconstructions enhanced with (a) 0, (b) 2, (c) 4, (d) 6, (e) 8, and (f) 10 DS shown along plots of (g) ϵ_d and (h) ϵ_ρ.

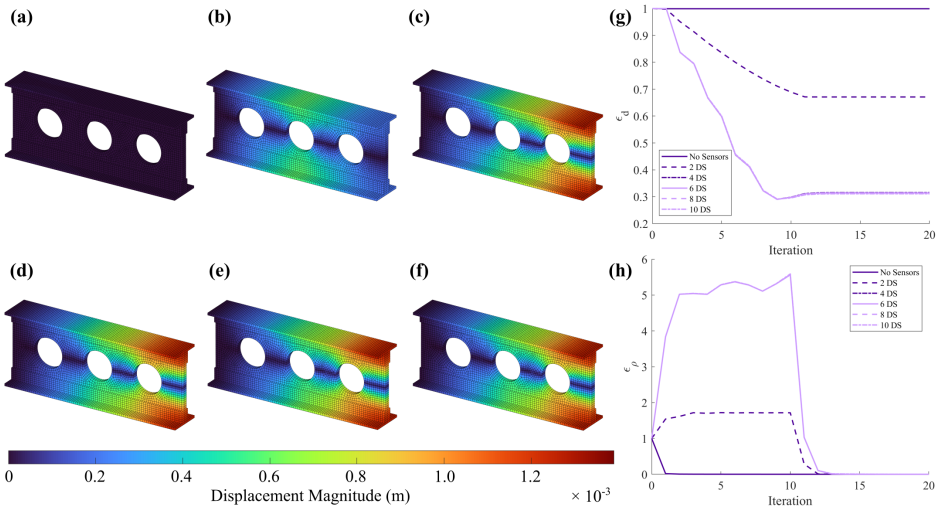

Figure 7: Wing spar displacement field reconstructions enhanced with (a) 0, (b) 2, (c) 4, (d) 6, (e) 8, and (f) 10 DS shown along plots of (g) ϵ_d and (h) ϵ_ρ.

The plots of ϵ_d^* against total number of DS in Figure 8 reinforce our visual observations quantitatively. The inclusion of relatively few DS undeniably yielded a major improvement in reconstruction accuracy, but after an early precipitous drop in ϵ_d^*, the returns diminished quickly. For the airfoil, there were notably two distinct drops in ϵ_d^*. The reason for the second drop at 10 DS is because the fifth set of 2 DS added was located furthest aft compared to the other DS, at approximately the location of the peak displacement magnitude according to the finite element solution. The 10 DS airfoil sensor configuration is shown in Figure 8(b). As more DS were added toward the root and tip of the airfoil further from areas of peak displacement, as seen in the 18 DS configuration, little additional improvement occurred. Thus, broadly speaking, DS tend to locally improve the reconstruction accuracy; therefore, a well populated and distributed DS configuration usually lends to a better reconstruction. Furthermore, it is especially advantageous to place DS in areas with large displacements relative to the rest of the shape.

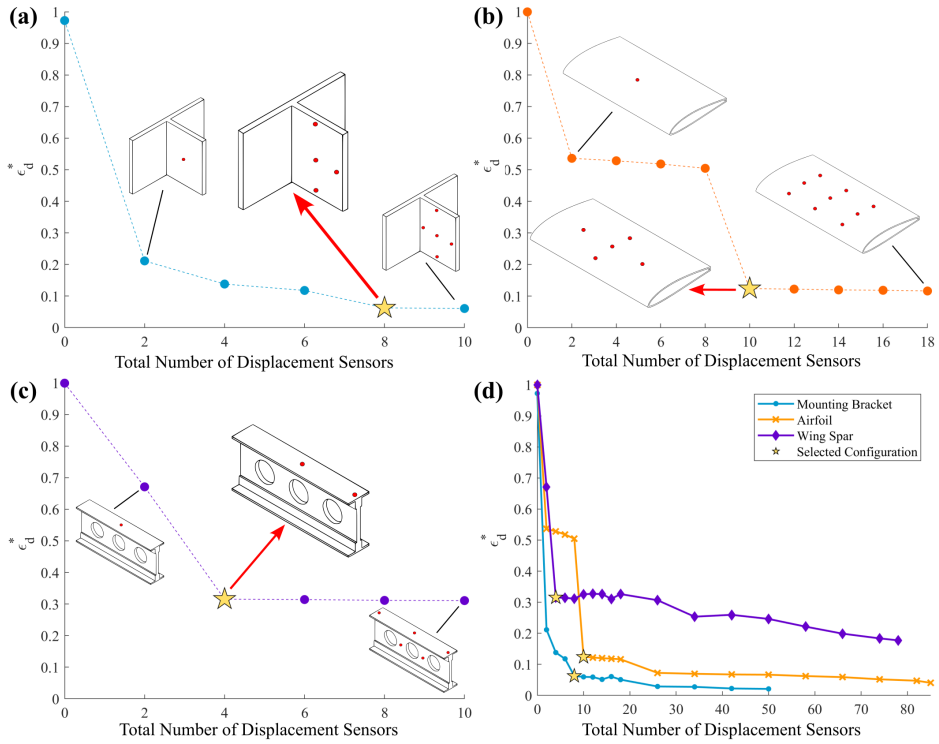

Figure 8: Plots of ϵ_d^* against total number of DS for the (a) mounting bracket, (b) airfoil, and (c) wing spar for a narrow range of sensor configurations. Corresponding illustrations of the sensor configuration are provided for selected points. The yellow star indicates the selected standard sensor configuration. (d) superimposes the ϵ_d^* plots for all three shapes, displaying the full range of sensor configurations.

To answer the question posed by the first objective, we considered one of the key challenges regarding instrumenting structures: determining the sensor configuration that maximizes efficiency and data utility while minimizing cost and complexity. Here, we took a simple approach by seeking the minimum number of sensors after which additional sensors do not appreciably improve the accuracy of the displacement reconstruction. In plot (d) of Figure 8, the relationship between the total number of sensors and ϵ_d^* for each shape resembles an 'L'-shaped curve. The corner of the curve roughly indicates the sensor configuration after which increasing the number of sensors yields diminishing improvement in reconstruction accuracy. Selecting the DS configuration at this corner,

we arrive at the 8 DS configuration for the mounting bracket, the 10 DS configuration for the airfoil, and the 4 DS configuration for the wing spar. The selected configurations are designated on the plots in Figure 8 by a yellow star. We refrain from enabling more quantitative techniques by defining a function modeling the relationship between ϵ_d^* and total number of DS because ϵ_d^* is deeply influenced by DS location and the load case. In other words, any function defined would generally not hold if the sensor locations or loading are changed.

Having seen the reconstruction results, we now comment on the convergence behavior of the SSIP. Figures 5–7 (g) and (h) plot ϵ_d and ϵ_ρ against iteration number, respectively, for each of the reconstructions shown. It can be seen that for all cases with DS, ϵ_d decreases steadily until the tenth iteration, after which ϵ_d plateaus. The approximately linear behavior is the result of the data ramping part of the resistivity-displacement SDF method. Once the data ramping was complete, the SSIP converged toward a stable solution, and ϵ_d quickly levels. The ϵ_ρ plot shows that ϵ_ρ converged to near zero for all cases displayed. This is a desired result because it indicates the SSIP successfully predicted a displacement field that gave rise to a resistivity distribution closely matching the simulated experimental resistivity distribution. However, ϵ_ρ converged in all cases despite each reconstructed displacement field being drastically different from each other and the finite element solution. This outcome demonstrates the underdetermined nature of the SSIP. In other words, the solution to the SSIP minimization is not unique, so many displacement fields can map to the same resistivity distribution. Consequently, the convergence of ϵ_ρ alone does not guarantee an accurate displacement reconstruction.

We can also observe that ϵ_ρ for cases with DS behaved more unstably compared cases without DS. For instance in mounting bracket, in cases with DS ϵ_ρ plateaued during the first ten iterations before converging toward zero after the tenth iteration, whereas the case without DS did not exhibit this behavior. For the wing spar and airfoil, ϵ_ρ actually increased during the first ten iterations with the presence of DS. This behavior can be attributed to the data ramping. During each iteration, the SSIP calculates a displacement field that satisfies the minimization. Then, when the resistivity-displacement SDF manually replaces the SSIP predicted values with measured displacement data, the new $\boldsymbol{d}^n$ is no longer the vector predicted by the SSIP that satisfied the minimization.

5.1.2. Computational Experiment 2

Using the DS configurations selected in Computational Experiment 1, we next attempted to recover the displacement field from resistivity data with 50, 40, and 30 dB SNR. The reconstructions and error plots are shown in Figures 9–11. It can be seen that DS allowed the displacement reconstructions to remain largely intact as resistivity data noise increased. Both the displacement magnitude and contours were well captured down to 30 dB SNR for the mounting bracket and wing spar. This is corroborated by the ϵ_d plots which show ϵ_d remaining generally stable at higher noise levels. For the airfoil, the reconstruction is entirely erroneous at 30 dB SNR. This is because at 30 dB SNR the signals attributed to deformation became saturated with noise—the airfoil strains were much smaller than the other shapes. ϵ_d for this case diverged, but it is expected to eventually stabilize because ϵ_ρ is gradually converging toward zero. ϵ_ρ for all cases overall behaved similarly to Computational Experiment 1. Cases with more resistivity data noise had a larger initial resistivity error compared to cases with less resistivity data noise, but the opposite trend is seen in the ϵ_ρ plots because ϵ_ρ is a normalized value. Nevertheless, the end behavior is more important because it is an indicator of whether or not the SSIP has converged to a solution.

Upon closer inspection, aberrations can be observed on reconstructions with higher noise levels. For instance, small displacements were predicted on the mounting bracket flange from the 30 dB resistivity data where there should be none. However, in general, noise aberrations are difficult to discern from a displacement magnitude map because noise tends to more negatively impact the

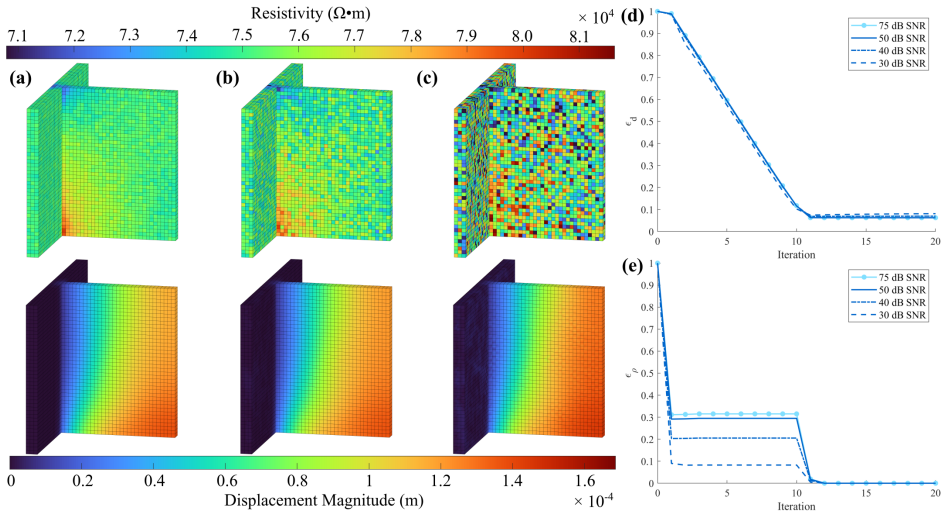

Figure 9: The mounting bracket displacement reconstructions (bottom row) from resistivity data (top row) with (a) 50 dB, (b) 40 dB, and (c) 30 dB SNR enhanced with 8 DS. Plots of (d) ϵ_d and (e) ϵ_ρ are given for each noise level, including the 75 dB case from Computational Experiment 1.

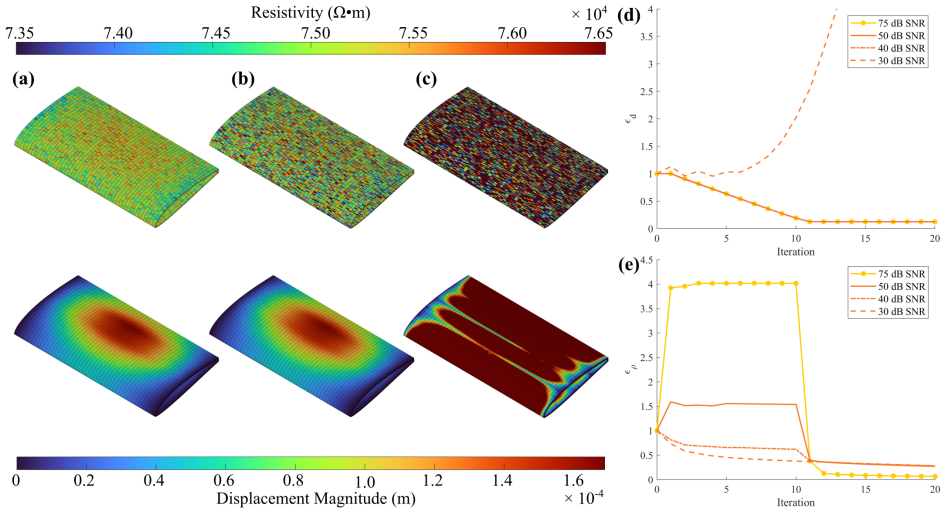

Figure 10: The airfoil displacement reconstructions (bottom row) from resistivity data (top row) with (a) 50 dB, (b) 40 dB, and (c) 30 dB SNR enhanced with 10 DS. Plots of (d) ϵ_d and (e) ϵ_ρ are given for each noise level, including the 75 dB case from Computational Experiment 1.

reconstruction of non-dominant displacement components more than the dominant components for DS enhanced reconstructions. The aberrations are in effect hidden by the accurate reconstruction of the dominant displacement component.

Overall, the results of this experiment demonstrate that resistivity-displacement SDF makes the SSIP more robust to increased noise in the resistivity data, allowing the SSIP to extract reasonably accurate reconstructions from resistivity data with 30 dB SNR in some cases.

5.1.3. Computational Experiment 3

Once again using the DS configurations from Computational Experiment 1, we attempted to recover the displacement field from resistivity data with outliers. It is immediately apparent from Figure 12 that outlier data posed a steeper challenge for the SSIP than noise. We can visually

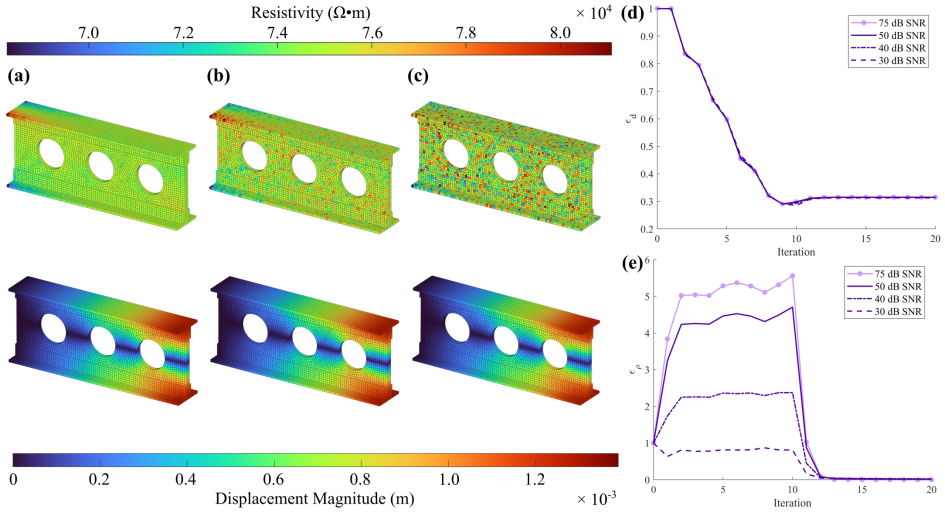

Figure 11: The wing spar displacement reconstructions (bottom row) from resistivity data (top row) with (a) 50 dB, (b) 40 dB, and (c) 30 dB SNR enhanced with 4 DS. Plots of (d) ϵ_d and (e) ϵ_ρ are given for each noise level, including the 75 dB case from Computational Experiment 1.

recognize that the mounting bracket and wing spar reconstructions are not physically correct, even without prior knowledge of the finite element solution. For the mounting bracket, the displacement magnitude was over-predicted, and significant aberrations skewed the contours of the displacement map. For the wing spar, the reconstructed displacement contours are most notably inaccurate on the left side of the rightmost circular cutout. Aside from this, the displacement magnitude was reasonably well captured. The outlier effects were much milder for the airfoil, with only minor aberrations visibly present local to the outlier data locations. The airfoil reconstruction was otherwise unchanged from the Computational Experiment 1 reconstruction.

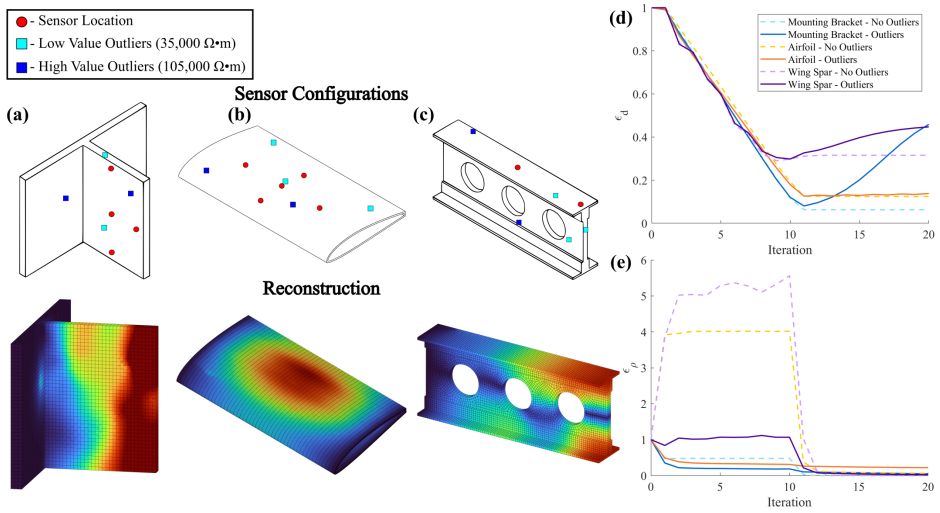

Figure 12: DS configurations used for the (a) mounting bracket, (b) airfoil, and (c) wing spar overlaid with locations of resistivity data outliers and their corresponding displacement reconstructions. The color scale of the correct solution for each shape is used. Plots of (d) ϵ_d and (e) ϵ_ρ compare the convergence behavior between the case with and without outliers.

In Figure 12(d), ϵ_d seemed to diverge for the mounting bracket and wing spar case with outliers.

The corresponding plots of ϵ_ρ however show convergence toward zero. The converging behavior of ϵ_ρ indicates that the SSIP will eventually arrive at a stable, albeit inaccurate, solution at a time beyond the iteration limit of 20. This once again demonstrates that while convergence of ϵ_ρ is an indicator that the SSIP has obtained a solution, it is not a good indicator whether the solution is accurate.

The conclusion drawn from this experiment is that resistivity-displacement SDF does not consistently allow the SSIP to obtain an accurate reconstruction from resistivity data with outliers. This inconsistency can be attributed to the randomness of the outlier data location, shape geometry, and magnitude of loading. Therefore, it may be more beneficial to apply minimization schemes more aptly designed to address outlier data in addition to SDF.

5.2. Resistivity-Strain Sensor Data Fusion Results

General guidance from iFEM literature regarding the selection of weight coefficients states that elements with strain data are to be assigned a weight coefficient that is roughly 1×10^3 to 1×10^6 larger than elements without strain data [53]. Regarding the selection of specific values for weight coefficients, no strict mathematical methodology has been established for the general case. Therefore, in our case, we selected a weight for the SS elements such that the corresponding entries of $\boldsymbol{K}$ became, on average, the same order of magnitude as the entries of the $\boldsymbol{G}$ matrix. Thus, a weight of 1×10^2 was assigned to SS elements of the mounting bracket and wing spar, and 1×10^8 for the airfoil. The weights for non-SS elements were 1×10^{-2} for the mounting bracket and wing spar, and 1×10^4 for the airfoil.

5.2.1. Computational Experiment 1

Figures 13–15 display reconstructions and error plots for each shape while increasing the number of SS. It can be observed visually that fusing additional strain data does improve the accuracy of the SSIP displacement field recovery overall, and the reconstructions become more accurate as the number of SS are increased. However, while the displacement field contours are reasonably well captured in all shapes, the displacement magnitude is under-predicted, even at the maximum sensor configuration. This is clearly seen by the fact that the colors of the reconstructions are far from the peak colors on the scale. To clarify, the color scale is the same as the scale used in the finite element solutions (i.e., the correct solutions that we seek as shown in Figure 4). Figure 16 shows that ϵ_d^* steadily decreases with increasing number of SS, but by very small increments with each new sensor set. The error plots show that the SSIP enhanced with resistivity-strain SDF exhibited very fast convergence toward a solution, with ϵ_d stabilizing ϵ_ρ converging toward zero within two iterations.

Out of the three shapes, the mounting bracket reconstructions come much closer to the correct solution than the airfoil and wing spar, seen both visually and Figure 16(d). This is potentially because many SS were located in regions of high strain and were aligned with the primary direction of deformation. For the mounting bracket, the SS were distributed uniformly on the web and measured the ε_{22}, ε_{33}, and ε_{23} strains; these strain components were also the dominant strain components resulting from the tension load. On the other hand, for the airfoil, ε_{22} and ε_{33} were the largest and concentrated at the fixed ends and the leading edge. The SS measured ε_{11}, ε_{33}, and ε_{13} and were mostly far from the fixed edges.

Compared to the results of resistivity-displacement SDF, resistivity-strain SDF did not attain as high a level of accuracy for the same number of sensors. However, resistivity-strain SDF does seem to possess an advantage over resistivity-displacement SDF in the ability to capture the displacement field contours. This can be seen most vividly in the case of the airfoil. Using 2 DS, the reconstruction was only accurate locally to the DS, whereas using 2 SS, although the displacement magnitude was

underpredicted, the contours throughout the entire shape were much truer to the finite element solution. This is likely because the resistivity-strain SDF method incorporates a global strain-displacement matrix in its formulation.

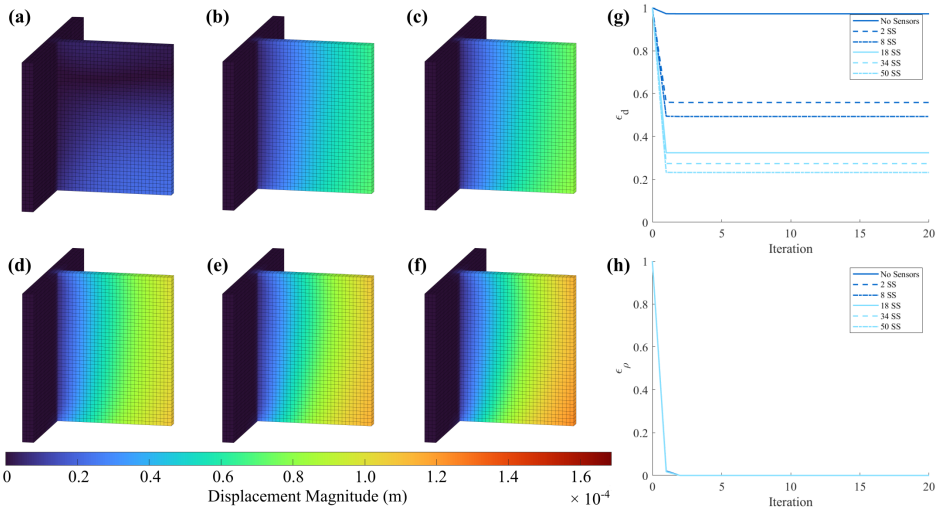

Figure 13: Mounting bracket displacement field reconstructions enhanced with (a) 0, (b) 2, (c) 8, (d) 18, (e) 34, and (f) 50 SS shown along plots of (g) ϵ_d and (h) ϵ_ρ.

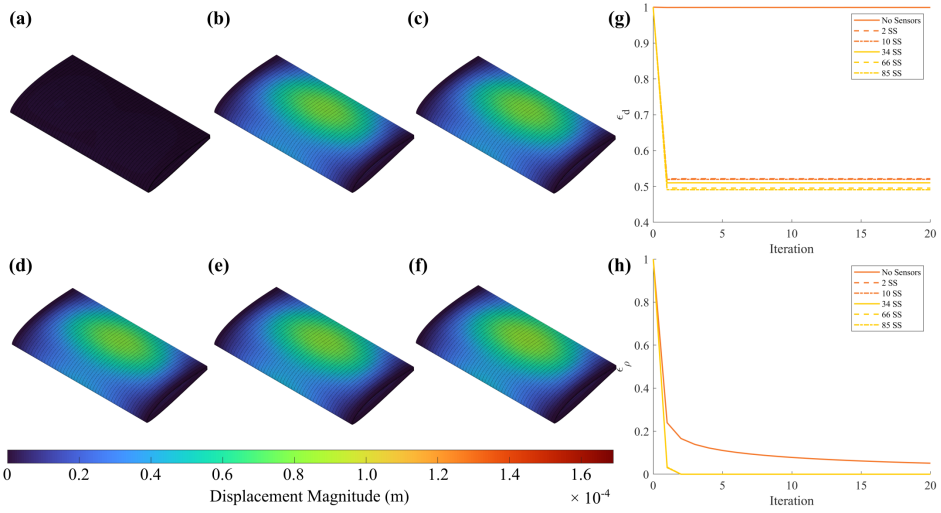

Figure 14: Airfoil displacement field reconstructions enhanced with (a) 0, (b) 2, (c) 10, (d) 34, (e) 66, and (f) 85 SS shown along plots of (g) ϵ_d and (h) ϵ_ρ.

We next select the SS configurations to satisfy the experiment objective using the plots in Figure 16. For the mounting bracket, a rough 'L'-shaped curve exists from which the 18 SS configuration is chosen. For the airfoil and wing spar, a corner occurs at the 2 SS configuration, with the rest of the curve being relatively flat. However, using only 2 SS is too few, especially considering the overall inaccuracy of the reconstructions at 2 SS and that the 18 SS configuration was selected for the mounting bracket—a notably less geometrically complex shape. By omitting the data point at 0 SS for both the airfoil and wing spar, what remained were curves with two corners. The SS configuration at the first corner was selected despite the higher ϵ_d^* because the overall change in ϵ_d^* is relatively small over the entire range of sensor configurations; thus, the 'more efficient' configuration

with fewer sensors was preferred. This would be the 34 SS configuration for the airfoil, and the 26 SS configuration for the wing spar.

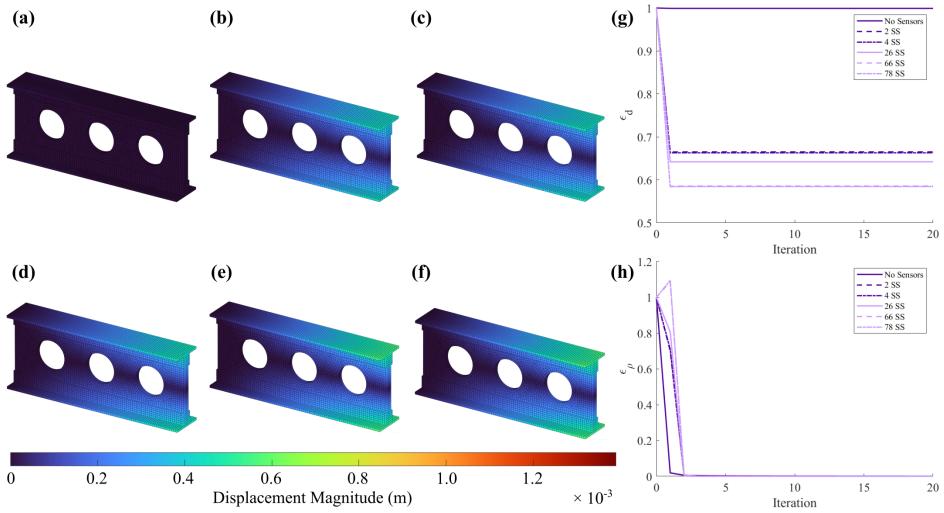

Figure 15: Wing spar displacement field reconstructions enhanced with (a) 0, (b) 2, (c) 4, (d) 26, (e) 66, and (f) 78 SS shown along plots of (g) ϵ_d and (h) ϵ_ρ.

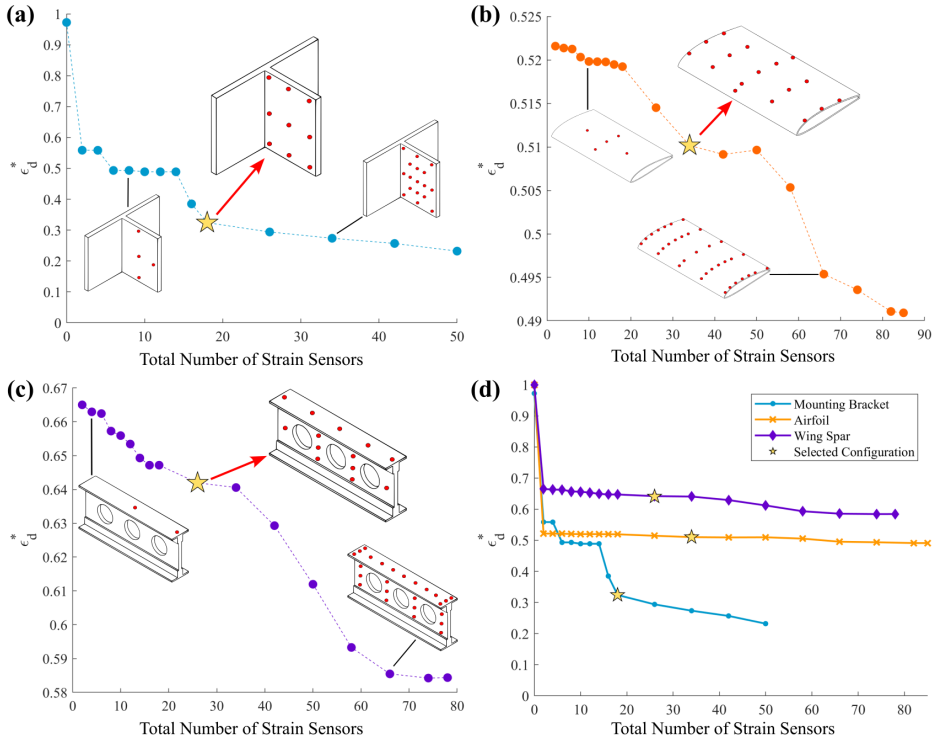

Figure 16: Plots of ϵ_d^* against total number of SS for the (a) mounting bracket, (b) airfoil, and (c) wing spar. Plots (b) and (c) omit the data point at 0 SS. Corresponding illustrations of the sensor configuration are provided for selected points. The yellow star indicates the selected standard sensor configuration. (d) superimposes the ϵ_d^* plots for all three shapes for the full range of sensor configurations.

5.2.2. *Computational Experiment 2*

Using the SS configurations from Computational Experiment 1, we next performed reconstructions with increased levels of resistivity noise. The reconstructions for all shapes were very poor at a SNR of 40 dB and below, as seen in Figures 17–19. The reconstructions at 50 dB SNR either remain generally unchanged, or the displacement magnitude were slightly more under-predicted compared to the 75 dB SNR case. Increasing the noise beyond 50 dB SNR caused skewing of the displacement field contours and severe over-prediction of the displacement magnitude. Overall, the results show that SS do make the SSIP more robust to noise in resistivity data up to around 50 dB SNR. Reconstructions become largely unreliable at a SNR below 50 dB.

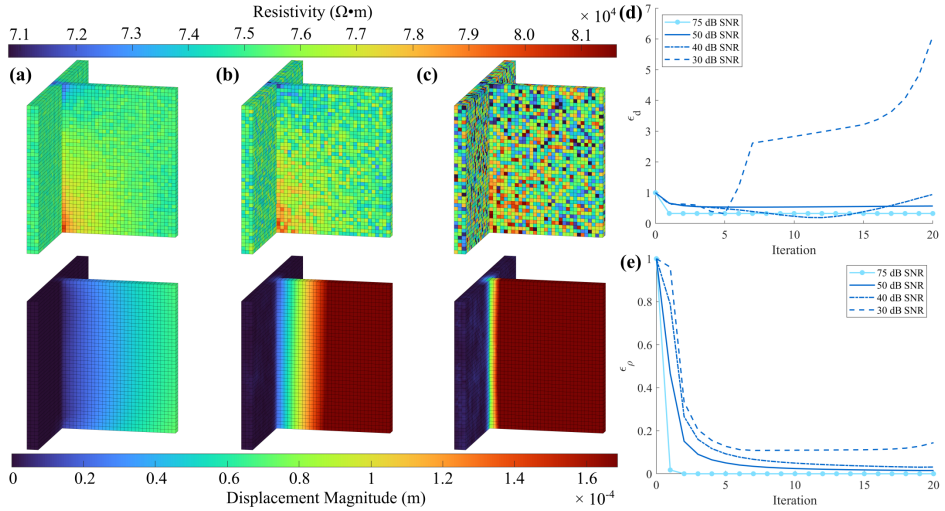

Figure 17: The mounting bracket displacement reconstructions (bottom row) from resistivity data (top row) with (a) 50 dB, (b) 40 dB, and (c) 30 dB SNR enhanced with 18 SS. Plots of (d) ϵ_d and (e) ϵ_ρ are given for each noise level, including the 75 dB case from Computational Experiment 1

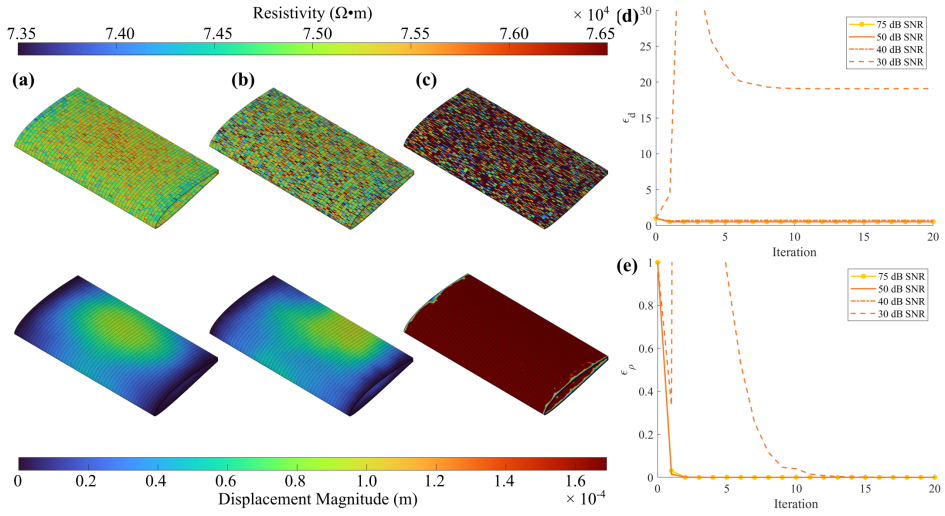

Figure 18: The airfoil displacement reconstructions (bottom row) from resistivity data (top row) with (a) 50 dB, (b) 40 dB, and (c) 30 dB SNR enhanced with 34 SS. Plots of (d) ϵ_d and (e) ϵ_ρ are given for each noise level, including the 75 dB case from Computational Experiment 1

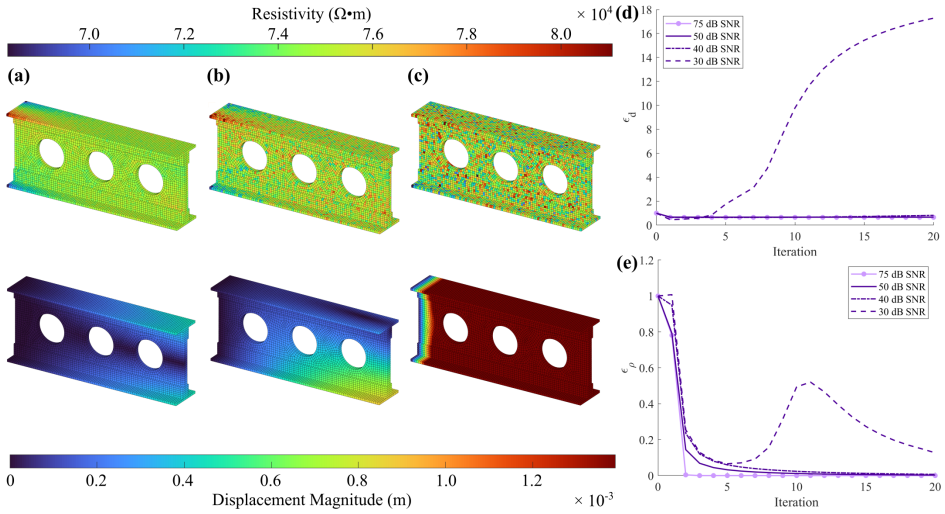

Figure 19: The wing spar displacement reconstructions (bottom row) from resistivity data (top row) with (a) 50 dB, (b) 40 dB, and (c) 30 dB SNR enhanced with 26 SS. Plots of (d) ϵ_d and (e) ϵ_ρ are given for each noise level, including the 75 dB case from Computational Experiment 1

5.2.3. Computational Experiment 3

When facing resistivity data with outliers, the SSIP enhanced with SS struggled to obtain accurate reconstructions. Figure 20 shows that in all cases, the displacement magnitudes were severely over-predicted, and the contours were entirely inaccurate. The plots of ϵ_ρ show that the reconstructions satisfy the SSIP minimization, but are clearly not the correct solution as indicated by the ϵ_d plots. From the results of this experiment, we conclude that resistivity-strain SDF does not allow the SSIP to accurately reconstruct the displacement field when the resistivity data contains outliers. Again, it may be advantageous to explore more outlier robust minimization schemes to counteract the effects of outlier data in conjunction with SDF.

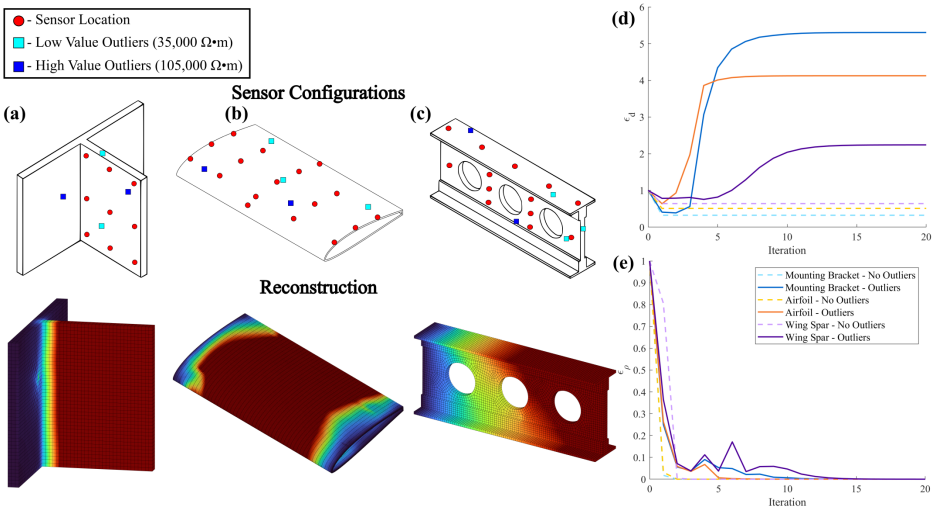

Figure 20: SS configurations used for the (a) mounting bracket, (b) airfoil, and (c) wing spar overlaid with locations of resistivity data outliers and their corresponding displacement reconstructions. The color scale of the correct solution for each shape is used. Plots of (d) ϵ_d and (e) ϵ_ρ compare the convergence behavior between the case with and without outliers.

6. Summary and Conclusions

In this article, we discussed how the ability of the SSIP to recover the displacement field of a deformed piezoresistive material from measured resistivity changes has significant implications for the advancement of CBM and MSA. However, more progress needed to be made in overcoming the mathematical limitations hindering its accuracy and proving its capacity to be applied to practical structures. We thus proposed that the accuracy of the SSIP and its applicability to more complex shapes could be improved by incorporating additional types of sensor data.

To this end, we developed two novel SDF methods that combine resistivity with displacement and strain data. These SDF methods were tested computationally. Three shapes approximating aircraft components were modeled virtually and subjected to loads. The resulting strain and displacement fields were calculated using standard finite element analysis, from which resistivity data was simulated. Then, three computational experiments were performed to qualitatively identify the number of sensors necessary to improve the SSIP displacement field recovery such that it reasonably matched the finite element solution and determine the impact of SDF when there is high noise and outliers in the resistivity data. The results show that both the fusion of displacement and strain data dramatically improve the SSIP accuracy. Relatively few DS were required to obtain a good reconstruction close to the correct solution. Using SS, the reconstructions did not come close to matching the correct solution due to under-prediction of the displacement magnitude, even when employing a large number of sensors, but still constituted a notable improvement over the original SSIP. Both DS and SS were shown to make the SSIP more robust to resistivity data noise, with DS allowing a reconstruction of reasonable quality to be extracted from data with 30 dB SNR in some cases, and SS for data with 50 dB SNR. When attempting to use resistivity data with outliers, the performance of SDF enhanced SSIP was inconsistent with DS and largely poor with SS.

The results also revealed several avenues for future investigation. First, the optimization of sensor placement could reduce the total number of sensors required for accurate reconstructions. Second, future work should explore more outlier-robust SSIP formulations, such as the 1-norm error minimization schemes solved via the primal-dual interior point method, in conjunction with SDF. Finally, the fusion of all three data types used in this work or the development of new SDF methods involving displacements, strains, or other data types should be considered in effort to minimize the total sensor count, since one of the key motivations of using self-sensing materials is to avoid cumbersome embedded sensor networks.

In conclusion, we believe that this initial exploration into enhancing the SSIP via SDF has demonstrated the viability of synergistically utilizing the SSIP with existing sensor technologies to advance the overall capability to gain insight into the mechanical state of piezoresistive materials. Continued advancement of techniques improving MSA of piezoresistive materials increases the feasibility of functional, self-sensing structures. Full realization of such capabilities can ultimately give rise to accurate, real-time condition monitoring of critical mechanical system components, entailing immense benefit for maintenance efficiency.

7. Acknowledgments

The authors gratefully thank the Air Force Office of Scientific Research Young Investigator Program (award number FA9550-23-1-0317) and the National Science Foundation CAREER Award (award number 2239039) for supporting this work.

References

[1] A. K. Jardine, D. Lin, D. Banjevic, A review on machinery diagnostics and prognostics implementing condition-based maintenance, Mechanical systems and signal processing 20 (7) (2006) 1483–1510.

[2] S. Pattabhiraman, C. Gogu, N. H. Kim, R. T. Haftka, C. Bes, Skipping unnecessary structural airframe maintenance using an on-board structural health monitoring system, Proceedings of the Institution of Mechanical Engineers, Part O: Journal of Risk and Reliability 226 (5) (2012) 549–560.

[3] Y. Li, S. Peng, Y. Li, W. Jiang, A review of condition-based maintenance: Its prognostic and operational aspects, Frontiers of Engineering Management 7 (3) (2020) 323.

[4] E. A. Meyer (Ed.), Proceedings of a Workshop on Materials State Awareness, The National Academies Press, Washington, DC, 2008.

[5] S. Laflamme, F. Ubertini, Back-to-basics: Self-sensing materials for nondestructive evaluation, 2019.

[6] B. R. Loyola, T. M. Briggs, L. Arronche, K. J. Loh, V. La Saponara, G. O'Bryan, J. L. Skinner, Detection of spatially distributed damage in fiber-reinforced polymer composites, Structural Health Monitoring 12 (2013) 225–239.

[7] T. Tallman, S. Gungor, K. Wang, C. Bakis, Tactile imaging and distributed strain sensing in highly flexible carbon nanofiber/polyurethane nanocomposites, Carbon 95 (2015) 485–493.

[8] A. Baltopoulos, N. Polydorides, L. Pambaguian, A. Vavouliotis, V. Kostopoulos, Exploiting carbon nanotube networks for damage assessment of fiber reinforced composites, Composites Part B: Engineering 76 (2015) 149–158.

[9] H. Dai, G. J. Gallo, T. Schumacher, E. T. Thostenson, A Novel Methodology for Spatial Damage Detection and Imaging Using a Distributed Carbon Nanotube-Based Composite Sensor Combined with Electrical Impedance Tomography, Journal of Nondestructive Evaluation 35 (2) (2016) 26.

[10] G. J. Gallo, E. T. Thostenson, Spatial damage detection in electrically anisotropic fiber-reinforced composites using carbon nanotube networks, Composite Structures 141 (2016) 14–23.

[11] W. Lestari, B. Pinto, V. La Saponara, J. Yasui, K. J. Loh, Sensing uniaxial tensile damage in fiber-reinforced polymer composites using electrical resistance tomography, Smart Materials and Structures 25 (8) (2016) 085016.

[12] S. Nonn, M. Schagerl, Y. Zhao, S. Gschossmann, C. Kralovec, Application of electrical impedance tomography to an anisotropic carbon fiber-reinforced polymer composite laminate for damage localization, Composites Science and Technology 160 (2018) 231–236.

[13] A. Thomas, J. Kim, T. Tallman, C. Bakis, Damage detection in self-sensing composite tubes via electrical impedance tomography, Composites Part B: Engineering 177 (2019) 107276.

[14] M. Sannamani, J. Gao, W. W. Chen, T. N. Tallman, Damage detection in non-planar carbon fiber-reinforced polymer laminates via electrical impedance tomography with surface-mounted electrodes and directional sensitivity matrices, Composites Science and Technology 224 (Jun. 2022).

[15] L. Homa, M. Sannamani, A. J. Thomas, T. N. Tallman, J. Wertz, Enhanced damage imaging in three-dimensional composite structures via electrical impedance tomography with mixed and level set regularization, NDT & E International 137 (2023) 102830.

[16] T.-C. Hou, K. J. Loh, J. P. Lynch, Spatial conductivity mapping of carbon nanotube composite thin films by electrical impedance tomography for sensing applications, Nanotechnology 18 (2007) 315501.

[17] K. J. Loh, T.-C. Hou, J. P. Lynch, N. A. Kotov, Carbon Nanotube Sensing Skins for Spatial Strain and Impact Damage Identification, Journal of Nondestructive Evaluation 28 (2009) 9–25.

[18] T.-C. Hou, J. P. Lynch, Electrical Impedance Tomographic Methods for Sensing Strain Fields and Crack Damage in Cementitious Structures, Journal of Intelligent Material Systems and Structures 20 (11) (2009) 1363–1379.

[19] K. Karhunen, A. Seppänen, A. Lehikoinen, P. J. Monteiro, J. P. Kaipio, Electrical resistance tomography imaging of concrete, Cement and Concrete Research 40 (1) (2010) 137–145.

[20] M. Hallaji, M. Pour-Ghaz, A new sensing skin for qualitative damage detection in concrete elements: Rapid difference imaging with electrical resistance tomography, NDT & E International 68 (2014) 13–21.

[21] M. Hallaji, A. Seppänen, M. Pour-Ghaz, Electrical resistance tomography to monitor unsaturated moisture flow in cementitious materials, Cement and Concrete Research 69 (2015) 10–18.

[22] D. Smyl, R. Rashetnia, A. Seppänen, M. Pour-Ghaz, Can Electrical Resistance Tomography be used for imaging unsaturated moisture flow in cement-based materials with discrete cracks?, Cement and Concrete Research 91 (2017) 61–72.

[23] D. Smyl, M. Pour-Ghaz, A. Seppänen, Detection and reconstruction of complex structural cracking patterns with electrical imaging, NDT & E International 99 (2018) 123–133.

[24] T. N. Tallman, K. W. Wang, An inverse methodology for calculating strains from conductivity changes in piezoresistive nanocomposites, Smart Materials and Structures 25 (11) (2016) 115046.

[25] T. Tallman, S. Gungor, G. Koo, C. Bakis, On the inverse determination of displacements, strains, and stresses in a carbon nanofiber/polyurethane nanocomposite from conductivity data obtained via electrical impedance tomography, Journal of Intelligent Material Systems and Structures 28 (18) (2017) 2617–2629.

[26] T. N. Tallman, Full-field mechanics imaging by direct inversion of electrical data, Proceedings of the Royal Society A: Mathematical, Physical and Engineering Sciences 481 (2319) (2025).

[27] H. Hassan, T. N. Tallman, Failure prediction in self-sensing nanocomposites via genetic algorithm-enabled piezoresistive inversion, Structural Health Monitoring 19 (3) (2020) 765–780.

[28] D. Hall, J. Llinas, An introduction to multisensor data fusion, Proceedings of the IEEE 85 (1) (1997) 6–23.

[29] F. E. White, Data Fusion Lexicon, Tech. rep., OSD or Non-Service DoD Agency, Fort Belvoir, VA (Oct. 1991).

[30] Y. Wu, E. Blasch, G. Chen, L. Bai, H. Ling, Multiple source data fusion via sparse representation for robust visual tracking, in: 14th International Conference on Information Fusion, IEEE, 2011, pp. 1–8.

[31] E. Blasch, Context aided sensor and human-based information fusion, in: NAECON 2014 - IEEE National Aerospace and Electronics Conference, IEEE, Dayton, OH, USA, 2014, pp. 127–134.

[32] E. Blasch, J. Nagy, A. Aved, E. K. Jones, W. M. Pottenger, A. Basharat, A. Hoogs, M. Schneider, R. Hammoud, G. Chen, et al., Context aided video-to-text information fusion, in: 17th International Conference on Information Fusion (FUSION), IEEE, 2014, pp. 1–8.

[33] Z. Liu, D. S. Forsyth, J. P. Komorowski, K. Hanasaki, T. Kirubarajan, Survey: State of the Art in NDE Data Fusion Techniques, IEEE Transactions on Instrumentation and Measurement 56 (6) (2007) 2435–2451.

[34] R.-T. Wu, M. R. Jahanshahi, Data fusion approaches for structural health monitoring and system identification: Past, present, and future, Structural Health Monitoring 19 (2) (2020) 552–586.

[35] W. Nsengiyumva, S. Zhong, M. Luo, Q. Zhang, J. Lin, Critical insights into the state-of-the-art nde data fusion techniques for the inspection of structural systems, Structural Control and Health Monitoring 29 (1) (2022) e2857.

[36] X. E. Gros, Applications of NDT data fusion, Springer, 2001.

[37] D. Horn, W. Mayo, Nde reliability gains from combining eddy-current and ultrasonic testing, NDT & E International - NDT E INT 33 (2000) 351–362.

[38] J. Moysan, A. Durocher, C. Gueudré, G. Corneloup, Improvement of the non-destructive evaluation of plasma facing components by data combination of infrared thermal images, NDT & E International 40 (6) (2007) 478–485.

[39] M.-A. Ploix, V. Garnier, D. Breysse, J. Moysan, NDE data fusion to improve the evaluation of concrete structures, NDT & E International 44 (5) (2011) 442–448.

[40] P. J. Dempsey, S. Sheng, Investigation of data fusion applied to health monitoring of wind turbine drivetrain components, Wind Energy 16 (4) (2013) 479–489.

[41] P. Lopato, G. Psuj, B. Szymanik, Nondestructive Inspection of Thin Basalt Fiber Reinforced Composites Using Combined Terahertz Imaging and Infrared Thermography, Advances in Materials Science and Engineering 2016 (2016) 1–13.

[42] S.-S. Jin, S. T. Kim, Y.-H. Park, Combining point and distributed strain sensor for complementary data-fusion: A multi-fidelity approach, Mechanical Systems and Signal Processing 157 (2021) 107725.

[43] J. Wertz, L. Homa, M. Cherry, S. O'Rourke, C. Flournoy, E. Blasch, A novel method for segmentation of titanium microtexture regions via sensor data fusion, Materials Characterization 210 (2024) 113770.

[44] D. Zonta, F. Bruschetta, R. Zandonini, M. Pozzi, M. Wang, B. Glisic, D. Inaudi, D. Posenato, Y. Zhao, Sensor Fusion on Structural Monitoring Data Analysis: Application to a Cable-Stayed Bridge, Key Engineering Materials 569-570 (2013) 812–819.

[45] R. Heideklang, P. Shokouhi, Multi-sensor image fusion at signal level for improved near-surface crack detection, NDT & E International 71 (2015) 16–22.

[46] S. Pashoutani, J. Zhu, C. Sim, K. Won, B. A. Mazzeo, W. S. Guthrie, Multi-sensor data collection and fusion using autoencoders in condition evaluation of concrete bridge decks, Journal of Infrastructure Preservation and Resilience 2 (2021) 1–12.

[47] H. Hassan, W. A. Crossley, T. N. Tallman, Hybrid optimization schemes for solving the piezoresistive inversion problem in self-sensing materials, Smart Materials and Structures 33 (2024) 065033.

[48] H. Hassan, T. N. Tallman, A comparison of metaheuristic algorithms for solving the piezoresistive inverse problem in self-sensing materials, IEEE Sensors Journal 21 (1) (2020) 659–666.

[49] G. Koo, T. Tallman, Higher-order resistivity-strain relations for self-sensing nanocomposites subject to general deformations, Composites Part B: Engineering 190 (2020) 107907.

[50] D. Holder, Institute of Physics (Great Britain) (Eds.), Electrical impedance tomography: methods, history, and applications, Series in medical physics and biomedical engineering, Institute of Physics Pub, 2005.

[51] A. Tessler, A variational principle for reconstruction of elastic deformations in shear deformable plates and shells, National Aeronautics and Space Administration, Langley Research Center, 2003.

[52] A. Tessler, J. L. Spangler, Inverse fem for full-field reconstruction of elastic deformations in shear deformable plates and shells, in: 2nd European workshop on structural health monitoring, 2004.

[53] A. Tessler, J. L. Spangler, M. Gherlone, M. Mattone, M. Di Sciuva, Real-time characterization of aerospace structures using onboard strain measurement technologies and inverse finite element method, in: Proceedings of the 8th international workshop on structural health monitoring, Vol. 2, Stanford Univ Stanford, CA, 2011, pp. 981–989.

[54] D. Poloni, D. Oboe, C. Sbarufatti, M. Giglio, Towards a stochastic inverse finite element method: A gaussian process strain extrapolation, Mechanical Systems and Signal Processing 189 (2023) 110056.

[55] D. Oboe, C. Sbarufatti, M. Giglio, Physics-based strain pre-extrapolation technique for inverse finite element method, Mechanical Systems and Signal Processing 177 (2022) 109167.

[56] M. Drela, XFOIL: An Analysis and Design System for Low Reynolds Number Airfoils, in: T. J. Mueller (Ed.), Low Reynolds Number Aerodynamics, Springer Berlin Heidelberg, Berlin, Heidelberg, 1989, pp. 1–12.

[57] G. M. Koo, On the development of macroscale modeling strategies for ac/dc transport-deformation coupling in self-sensing piezoresistive materials, Phd thesis, Purdue University, School of Aeronautics and Astronautics (2020).